6.1. Synthesis of FePt Nanoparticles

The synthesis of FePt alloy nanoparticles is based on the reduction of Pt(acac)$_2$ and Fe(acac)$_2$ (acac=acetylacetonate, $CH_3COCHCH_3$) in a high temperature solutions. In the present investigation, a slight modification was done by adding 1,2-hexadecanediol to reduce platinum precursor to pt metal. The composition and size of formed alloy nanoparticles can be controlled by varying the reaction temperature along with molar ratio of platinum and iron precursor.

6.1.1. Risk Analysis

Risk analysis includes evaluation of the qualitative or quantitative process of linking the likelihood of occurrence and severity of harm and the ability to detect the harm. For identifying critical processing variables, Ishikawa diagram/cause and effect diagram was used. Ishikawa diagrams were constructed to establish relation between the processing/formulation variables and characteristics affected in order to identify the potential risk affecting quality attributes. The failure mode effect analysis (FMEA) method was used for qualitative risk assessment [1]. FMEA helps to identify the factors which can cause failure of product from meeting the desired QTPP (Quality Target Product Profile). The risk analysis (FMEA) was done by organizing all the probable factors using Ishikawa diagram or fish bone diagram. Ishikawa diagram (Figure 6.1) shows all the possible factors which can directly or indirectly affect the final product quality attributes which in the present case was particle size and atomic composition. In order to select factors having maximum effect on quality attributes of final product, IRMA and RPN methodology was adopted. The IRMA (Initial Risk based Matrix Analysis) study helps in preliminary screening of factors from Ishikawa diagram. IRMA categorizes factor on the basis of risk. Factors falling under category of high risk were evaluated using RPN (Risk Priority Numbering) methodology which includes assigning of values to each factor on the basis of their severity, occurrence and detection [2]. RPN was calculated by multiplying the severity rating (S) with that of occurrence rating (O) and the detection rating (D). Priority order of factors falling under category of critical variables was done on the basis of final RPN calculation (Table 6.1). Preliminary investigation was done for the factors having high RPN. Five factors, namely molar ratioof Pt(acac)$_2$ and Fe(acac)$_2$(X1), oleic acid:oleylamine (X2), 1,2-hexadecanediol (X3), reflux temperature (X4), reflux time (X5), were selected for further optimization study. Two responses were studied, particle size and atomic composition.

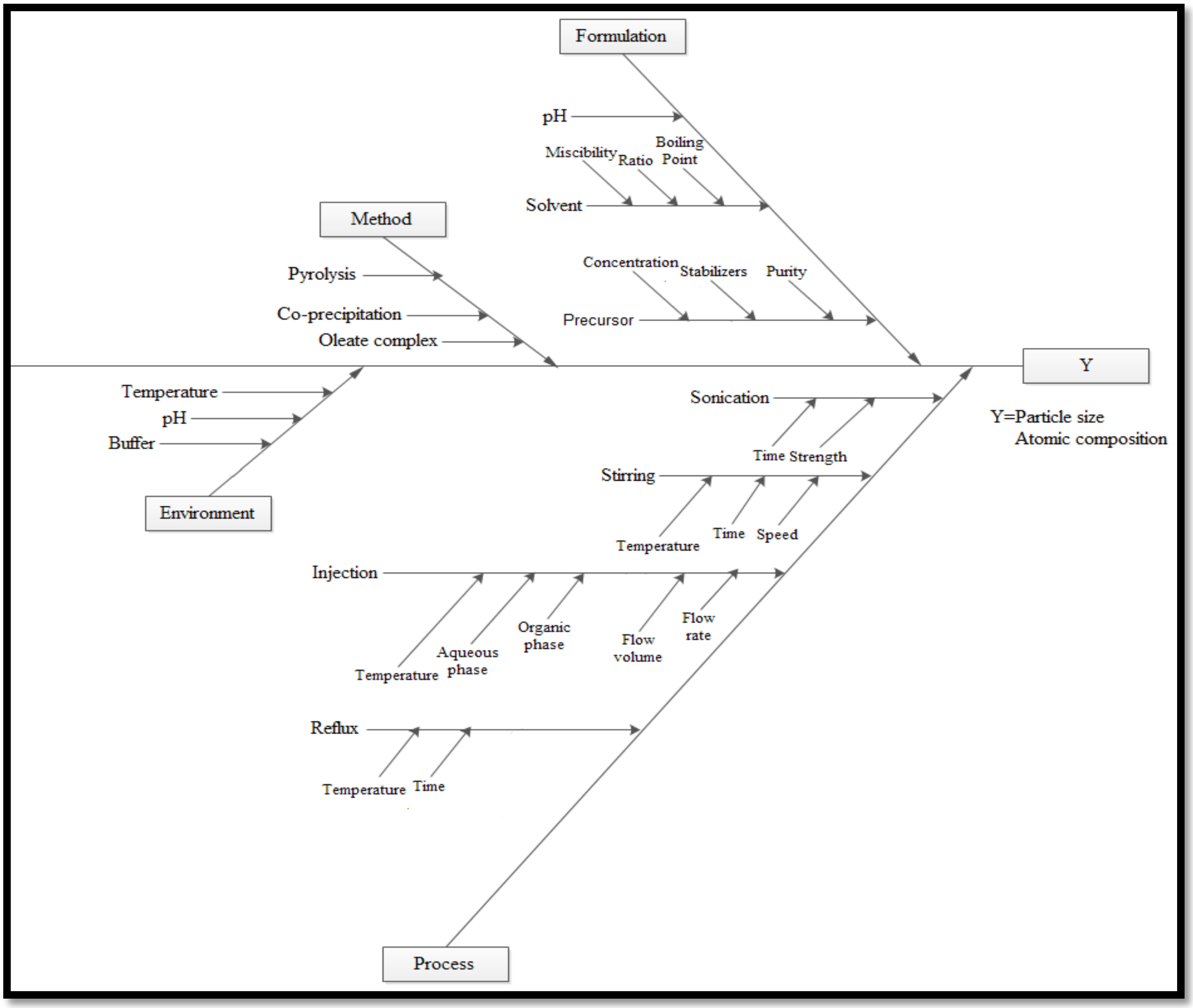

Figure 6.1: Ishikawa diagram for selection of factors

6.1.2. Preliminary investigation of critical variables

A preliminary study was done to optimize the reaction condition so as to select conditions which could provide alloy nanoparticles with desired quality attributes. During preliminary study effect of the various reaction conditions i.e. reaction temperature, reflux time, molar ratio of precursor, surfactant, co-surfactant and reducing agent (1,2-hexadecanediol) on size and composition of synthesized alloy nanoparticles was studied and analyzed using SAS JMP.

Table 6.1**:** RPN of selected factors for selection of critical variables

Sr. No.	**Failure mode**	**S***	**O**	**D**	**RPN**	**Failure effect**
1	Precursor conc.	5	5	4	100	Particle size, atomic composition
2	Stabilizer conc.	4	4	5	80	Particle size, stability
3	Reflux temp.	4	5	4	80	Particle size, atomic composition
4	Reflux time	4	4	4	64	Atomic composition, PDI
5	1,2-hexadecanediol	5	4	3	60	atomic composition, particle size
6	Volume of reaction mixture	3	2	1	6	PDI
7	Injection rate	3	2	2	12	Particle size
8	pH	3	2	2	12	Particle size
9	Solvent	4	2	2	16	Atomic composition, particle size
10	Stirring time	3	1	2	6	Particle size, PDI
11	Stirring speed	3	1	2	5	Particle size, PDI

*S=severity rating; O=occurrence rating; D=detection rating

Initially, the effect ratio of oleic acid to oleylamine was investigated as they stabilize the synthesized FePt nanoparticles. During formation of nanoparticles, these stabilizers get reversibly absorbed on the organic shell and stabilize the nanoparticles mediating their growth. Surfactants like oleic acid that bind more tightly to nanoparticle surface provide greater steric hindrance, thus slowing the rate of material addition on nanoparticles seed resulting in smaller average size of nanoparticles [3].

Reflux temperature and reflux time was found to affect both size and composition of FePt nanoparticles (Figure 6.2). At lower temperature and higher reflux time, FePt nanoparticles with higher particle size were obtained. With increase in temperature from 240 ^{0}C to 320 ^{0}C, a decrease in particle size was observed. This variation can be explained on the basis of kinetically controlled growth process according to which if the growth rate (V) of two planes (facet) is different which normally happens at lower temperature, the growth along one facet will go on decreasing and vanish at particular leading to formation of non-spherical shape [4]. To form spherical nanoparticles, the free energies of different facets needs to be controlled which in this case is done by using oleic acid and oleylamine as surface stabilizing agents. But even after using surface stabilizing agents, the surface energies of one facet remains higher than another leading to formation of non spherical and particles with higher particle size. On increasing the reaction temperature to 320 ^{0}C, the system goes through energy evolution to new stable state driving anisotropic particles into isotropic which causes dissolution of corners of planes leading to formation of spherically shaped nanoparticles [5].

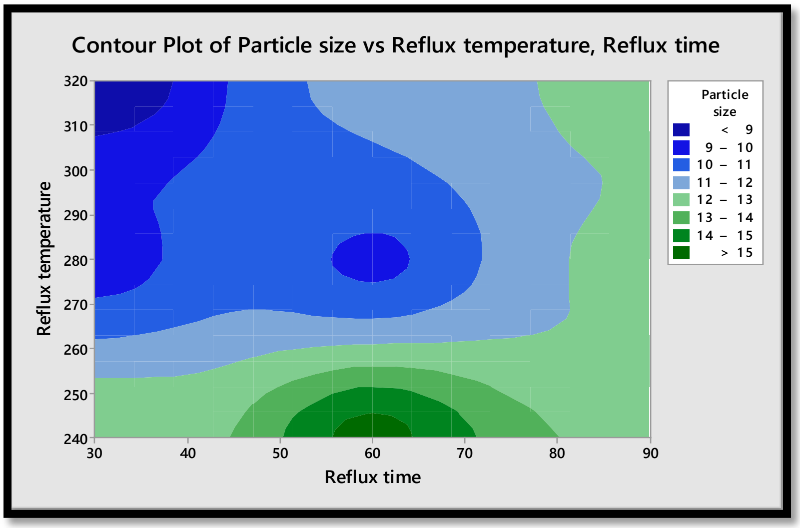

Figure 6.2**:**Preliminary investigation for effect of reflux temperature and time on particle size

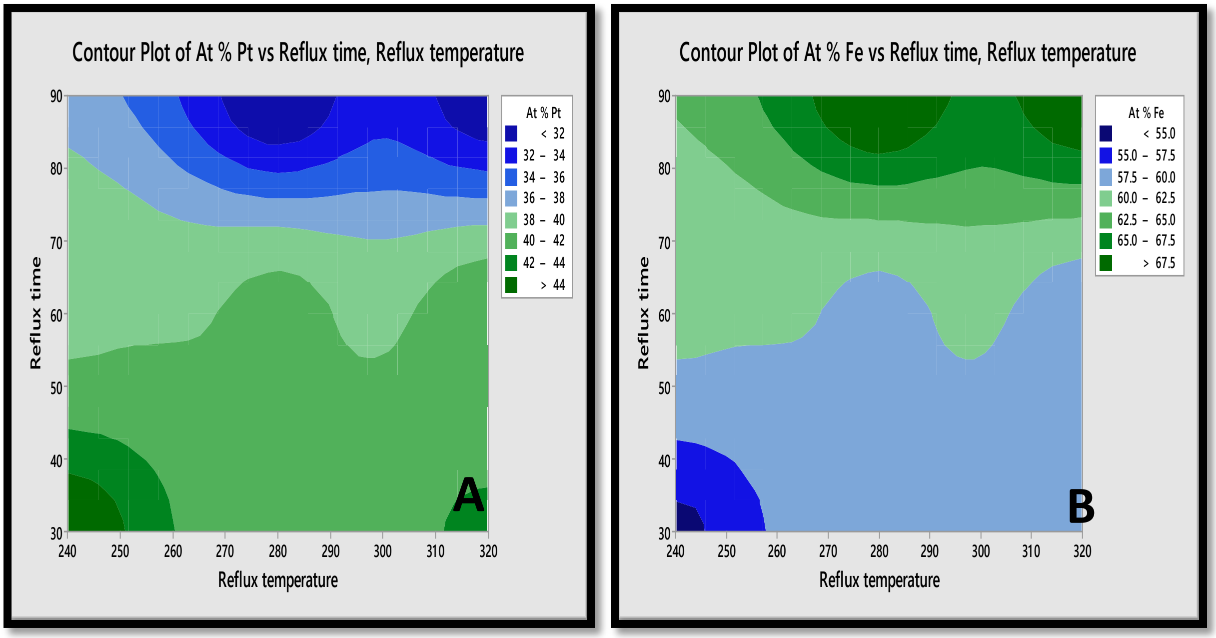

Figure 6.3:Effect of (A) reflux time and temperature on platinum atomic composition (At% Pt) in FePt nanoparticles; (B)reflux time and temperature on platinum atomic composition (At% Fe) in FePt nanoparticles

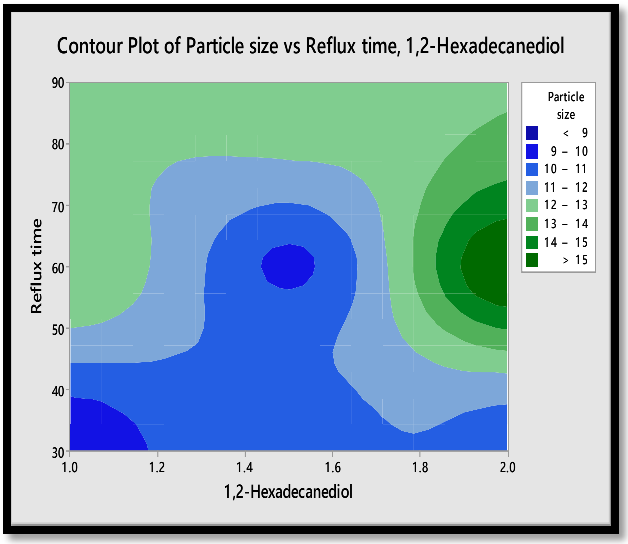
Contour Plot of Particle size vs Reflux time, 1,2-Hexadecanediol
Reflux time
30
40
50
60
70
80
90
1,2-Hexadecanediol
1.0
1.2
1.4
1.6
1.8
2.0
Particle size
< 9
9 – 10
10 – 11
11 – 12
12 – 13
13 – 14
14 – 15
> 15

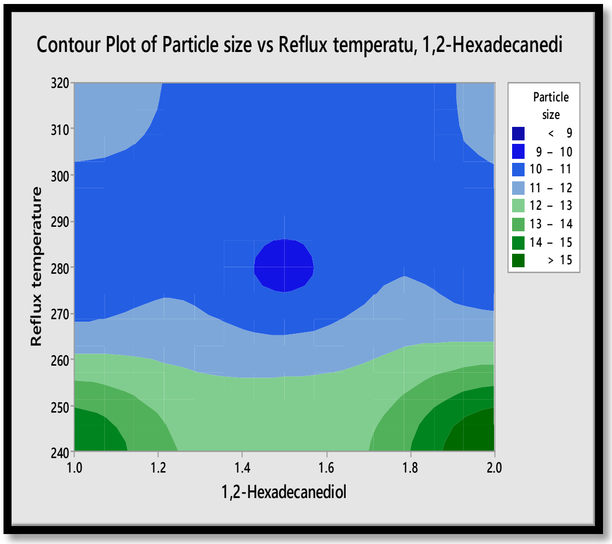
Contour Plot of Particle size vs Reflux temperatu, 1,2-Hexadecanedi
Reflux temperature
240
250
260
270
280
290
300
310
320
1,2-Hexadecanediol
1.0
1.2
1.4
1.6
1.8
2.0
Particle size
< 9
9 – 10
10 – 11
11 – 12
12 – 13
13 – 14
14 – 15
> 15

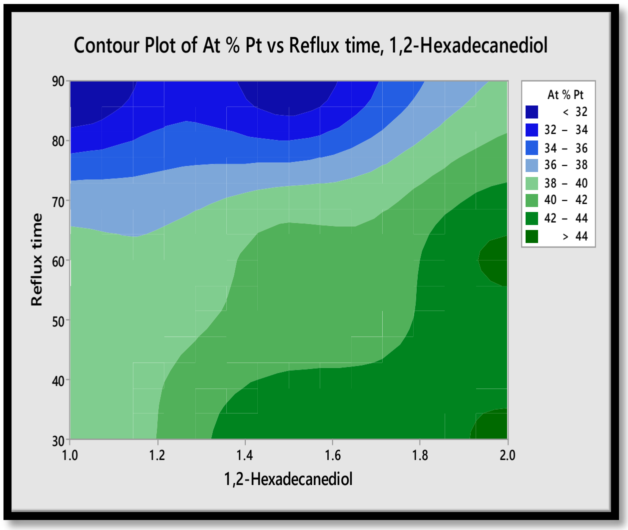
Contour Plot of At % Pt vs Reflux time, 1,2-Hexadecanediol
Reflux time
30
40
50
60
70
80
90
1,2-Hexadecanediol
1.0
1.2
1.4
1.6
1.8
2.0
At % Pt
< 32
32 – 34
34 – 36
36 – 38
38 – 40
40 – 42
42 – 44
> 44

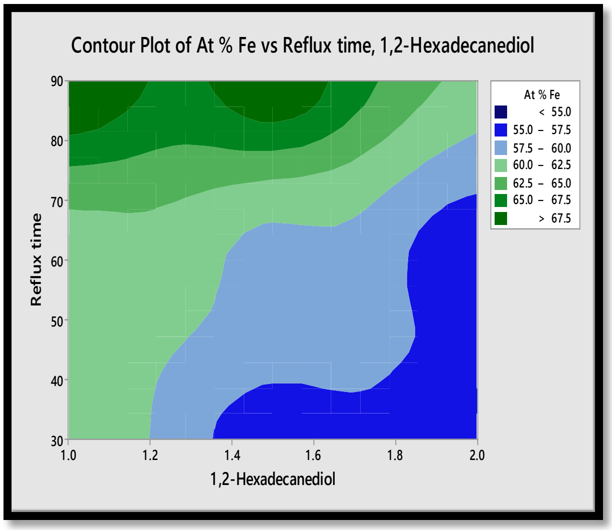
Contour Plot of At % Fe vs Reflux time, 1,2-Hexadecanediol
Reflux time
30
40
50
60
70
80
90
1,2-Hexadecanediol
1.0
1.2
1.4
1.6
1.8
2.0
At % Fe
< 55.0
55.0 – 57.5
57.5 – 60.0
60.0 – 62.5
62.5 – 65.0
65.0 – 67.5
> 67.5

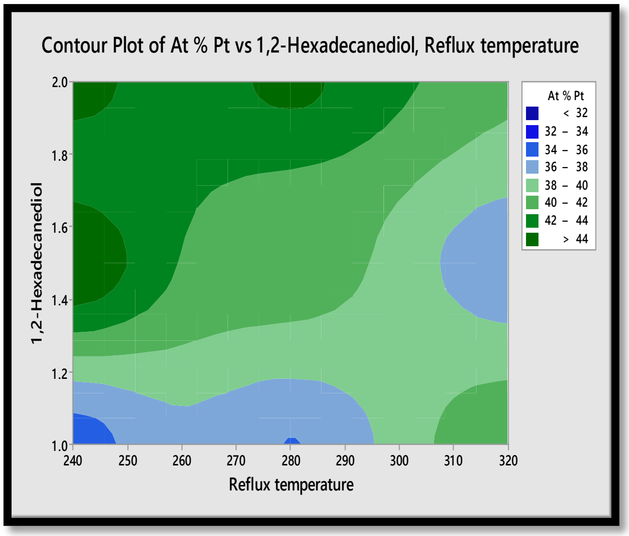
Contour Plot of At % Pt vs 1,2-Hexadecanediol, Reflux temperature
1,2-Hexadecanediol
1.0
1.2
1.4
1.6
1.8
2.0
Reflux temperature
240
250
260
270
280
290
300
310
320
At % Pt
< 32
32 – 34
34 – 36
36 – 38
38 – 40
40 – 42
42 – 44
> 44

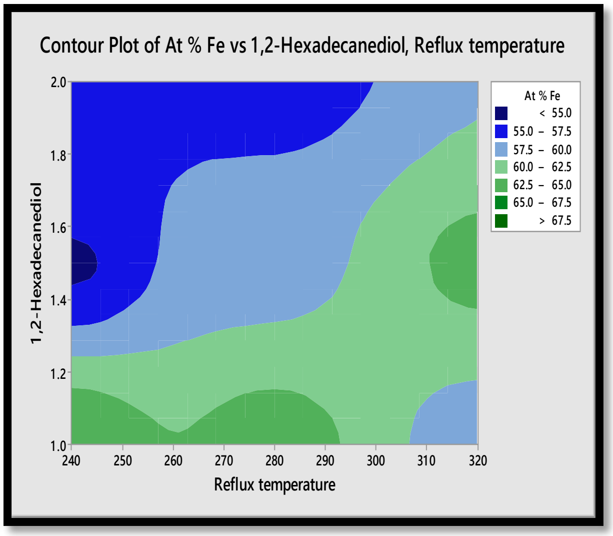
Contour Plot of At % Fe vs 1,2-Hexadecanediol, Reflux temperature
1,2-Hexadecanediol
1.0
1.2
1.4
1.6
1.8
2.0
Reflux temperature
240
250
260
270
280
290
300
310
320
At % Fe
< 55.0
55.0 – 57.5
57.5 – 60.0
60.0 – 62.5
62.5 – 65.0
65.0 – 67.5
> 67.5

Figure 6.4: Effect of (A) 1,2-Hexadecanediol and reflux time on particle size; (B); 1,2-Hexadecanediol and reflux temperature on particle size; (C) 1,2-Hexadecanediol and reflux time on atomic composition of Pt (At% Pt); (D)1,2-Hexadecanediol and reflux timeatomic composition of Fe (At% Fe); (E) 1,2-Hexadecanediol and reflux temperature on atomic composition of Pt (At% Pt); (F)1,2-Hexadecanediol and reflux temperature atomic composition of Fe (At% Fe) in FePt nanoparticles.

Another reason for increase in particle size can be attributed to the fact that during seeding process, migrating atom finds a defect site on crystal face where it can interact with large number of neighboring sites [6]. At lower temperature the metallic atoms are not able to reach near the top of convex face immediately leading to preferential growth along particular direction [6]. In case of atomic composition, an increase in atomic composition of Fe was observed with increase in reflux temperature and reflux time **(**Figure6.3**).** This might be due to increase in release of Fe atoms from precursor and attachment to the surface of FePt leading to increase in atomic composition as well as particle size [7].

The molar concentration of 1,2-hexadecanediol also affected both atomic composition and particle size of synthesized nanoparticles (Figure 6.4). With increase in concentration of 1,2-hexadecanediol, increase in particle size was observed which may be correlated to the fact that 1,2-hexadecanediol reduces platinum precursor to form Pt (platinum) seeds on which Fe (Iron) atoms get deposited. At higher concentration, large Pt seeds are formed which ultimately leads to formation of large and Pt rich FePt nanoparticles. With increase in temperature, weak connection between Fe atoms and surface of FePt nanoparticles is removed leading to formation of FePt nanoparticles with more homogeneous atomic composition. With increase in reflux time and temperature, increase in Fe atomic composition was observed.

Based on preliminary investigation, an optimum reaction condition range was obtained to synthesize FePt nanoparticles with controlled particle size and controlled atomic composition (1:1 atomic ratio) (Table 6.2)

Table 6.2**:** Working range of selected factors for synthesis of FePt nanoparticles

Sr. No.	**Reaction condition**	**Operating range**
1	Molar ratio of precursors (Fe:Pt)	2:1-2.5:1 mmol
2	Oleic acid:oleylamine	1:0.75-1.2:1 mmol
3	1,2-Hexadecanediol	1.4-1.6 mmol
4	Reflux temperature	265-320 °C
5	Reflux time	30-45 min

6.1.3. Optimization of FePt nanoparticles: Box–Behnken response surface methodology

Response surface methodology (RSM) is a group of statistical and mathematical method which is useful for the modeling and analyzing formulation problems. The main objective of this technique is to optimize the response surface that is influenced by various process parameters [8]. Response surface methodology also quantifies the relationship between the controllable input parameters and the obtained response surfaces. Box–Behnken design (BBD) is rotatable or nearly rotatable second-order designs based on three-level incomplete factorial designs. In this study, a three variable Box–Behnken response surface methodology **(**BB-RSM) was used to study the combined effect of molar ratio of Fe:Pt (X1),1,2-hexadecanediol (X2) and reflux temperature (X3) over three levels based on RPN analysis and preliminary investigation. The BB design is suitable for investigating quadratic response surfaces and generates a second degree polynomial model, which in turn is used in optimizing a process using a small number of experimental runs. The coded and actual values of the variables of BB-RSM are as shown in Table 6.3.

Table 6.3**:** Experimental runs obtained using BBD

Run	**X1**	**X2**	**X3**	**Y1**	**Y2**	**Y3**
F1	2	1.6	292.5	12.1±1.1	43±2.1	57±2.1
F2	2	1.5	320	5.7±0.9	57±2.3	43±2.1
F3	2.25	1.6	320	7.4±1.2	51±1.9	49±1.9
F4	2.5	1.6	292.5	11.4±1.2	55±1.7	45±2.3
F5	2.25	1.4	320	6.1±1.1	54±2.1	46±2.3
F6	2.5	1.5	265	14.3±1.3	69±2.5	31±1.7
F7	2.25	1.5	292.5	9.3±1.1	65±2.5	35±1.5
F8	2.25	1.5	292.5	9.3±1.1	65±2.5	35±1.5
F9	2.25	1.4	265	12.6±1.3	62±2.1	38±1.9
F10	2	1.4	292.5	10.1±1.2	58±1.7	42±2.1
F11	2.5	1.5	320	5.9±1.0	56±2.5	44±2.3
F12	2.25	1.6	265	17.2±1.5	59±2.3	41±2.6
F13	2.25	1.5	292.5	9.3±1.1	65±2.1	35±1.9
F14	2	1.5	265	14.5±1.4	61±2.3	39±1.7
F15	2.5	1.4	292.5	10.5±1.3	59±1.9	41±2.4

Where, X1= molar ratio of Fe:Pt precursors; X2= concentration of 1,2-hexadecanediol; X3=reflux temperature; Y1=particle size (nm); Y2=atomic composition of Fe (%); Y3=atomic composition of Pt (%).

6.1.3.1. Effect of independent variables on particle size

The obtained particle size for each formulation batch can be observed from Table 6.3 The particle size varied from 5.7±0.8 nm (F2) to 17.2±1.1 nm (F12) which shows that combination of critical formulation variables affect the particle size of nanoparticles. Half normal plots show that X2 and X3 were having most significant effect on Y1 (Fig.6.5).From the statistical analysis (Fig. 6.6), we can observe that the R^2 value for actual v/s predicted values of Y1 (particle size) was 0.99 which is a good correlation. Among two variables affecting particle size, X3 (p value<0.0001) demonstrated maximum effect on particle size followed by X2 (p value=0.0015), while X1 didn’t show any significant effect on particle size. The interaction of X2 and X3 also demonstrated significant effect on Y1 (p value =0.0211). Overall effect analysis of variables was also found to be significant (p value<0.001 (Figure 6.7). The obtained results from effect analysis of critical variables show that the factor exerts both positive and negative effect on response. The estimate for X3 was found to be -4.187 which demonstrated that an increase in the value of X3 will lead to decrease in Y1 i.e. particle size and vice versa. In case of X2, parameter estimate was 1.1 which means an increase in value of X2 will cause increase in value of Y1 and vice versa. The interaction between X1*X2 and X2*X3 was negative, although X2 independently exerted positive effect of Y1.

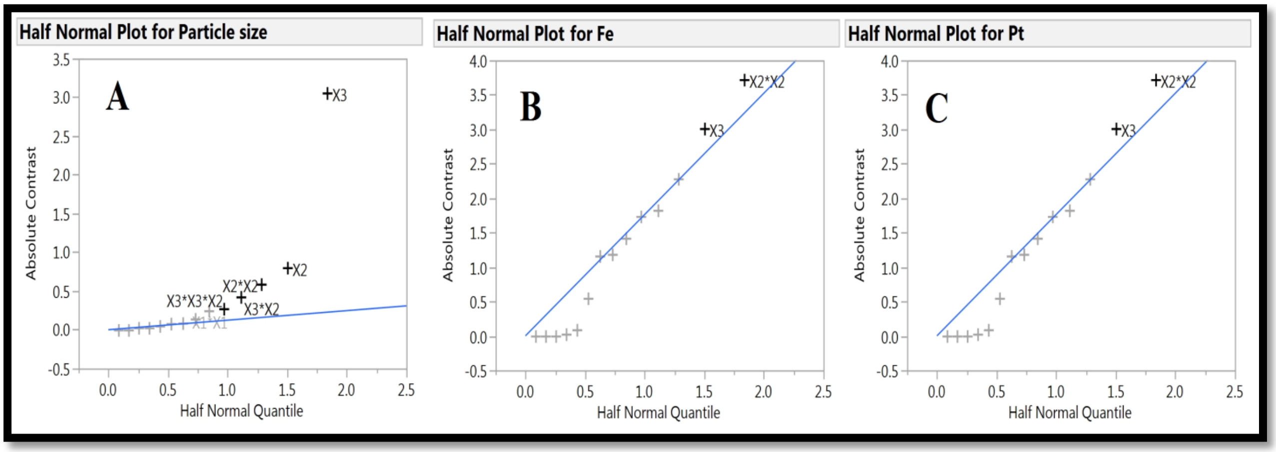

Figure 6.5**:** Half normal plot obtained for Y1 (A),Y2 (B) and Y3 (C) for synthesized FePt nanoparticles

The result of ANOVA proves that the model was significant for effect of selected variables on particle size with p value < 0.0001. The obtained results can be observed visually in the contour plots shown in Fig. 6.8 We can observe that with increase in X1, no significant increase in particle size was observed which is in accordance with effect analysis of variables on particle size and effect model obtained from design. In case of X2, a prominent effect was observed on particle size. An increase in particle size can be observed with increase in value of X2. In case of X3, increase in particle size was observed with increase in value of X3. The contour plot (Figure 6.8) between X1 and X2 shows that although the effect of X1 was not significant on Y1, at X2 value less than 1.5, slight decrease in Y1 was observed followed by slight increase in Y1 after X1 value of 2.26.

6.1.3.2. Effect of independent variables on atomic composition

The observed atomic composition for each formulation batch can be observed from Table 6.2. The atomic composition varied from 43%±2.1% (F1) to 69%±2.7%(F6) for Fe and 31%±1.9% (F6) to 57%±2.5% (F1) for Pt which shows that combination of critical formulation variables affect the atomic composition(Y2, Y3) of FePt nanoparticles. From the statistical analysis, we can observe that the R^2 value for actual v/s predicted values of Fe% (Y2) was 0.96 and 0.99 for Pt%(Y3) which shows a good correlation (Figure 6.6).

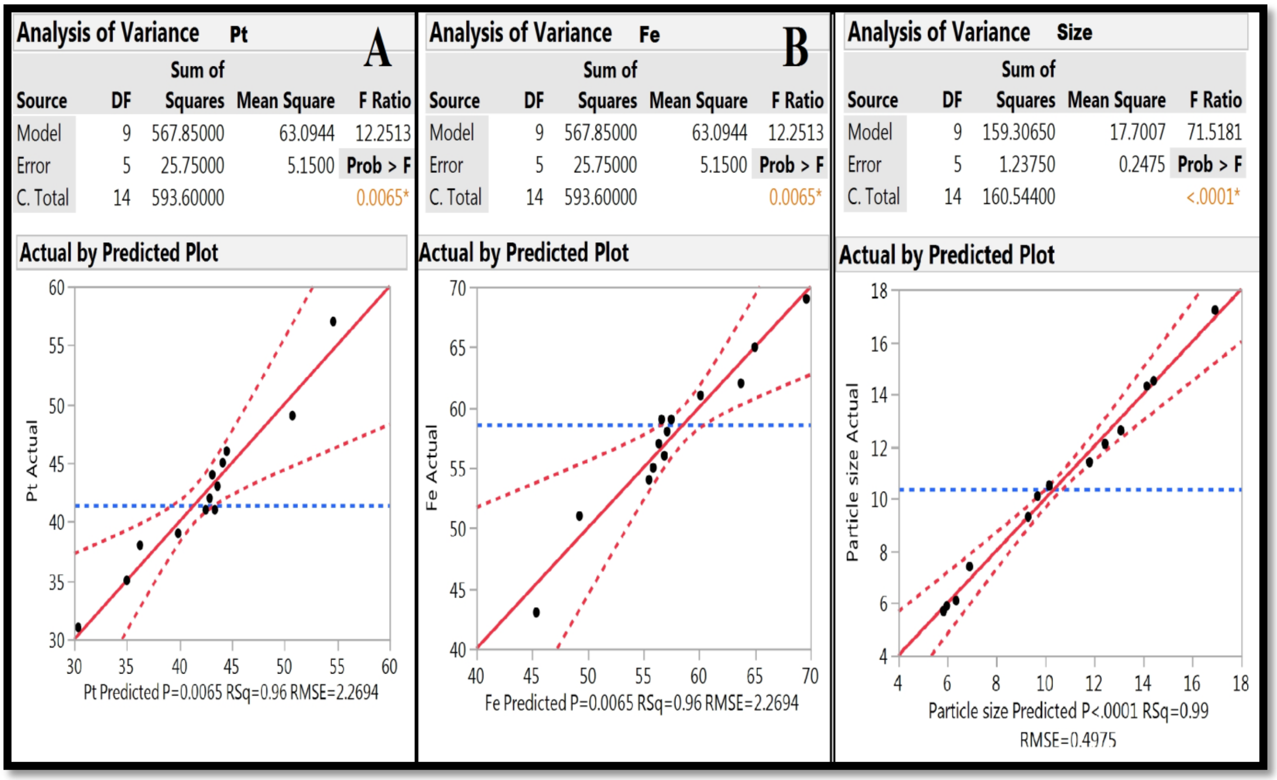

Analysis of Variance Pt

Source	DF	Sum of Squares	Mean Square	F Ratio
Model	9	567.85000	63.0944	12.2513
Error	5	25.75000	5.1500	Prob > F
C. Total	14	593.60000		0.0065*

Analysis of Variance Fe

Source	DF	Sum of Squares	Mean Square	F Ratio
Model	9	567.85000	63.0944	12.2513
Error	5	25.75000	5.1500	Prob > F
C. Total	14	593.60000		0.0065*

Analysis of Variance Size

Source	DF	Sum of Squares	Mean Square	F Ratio
Model	9	159.30650	17.7007	71.5181
Error	5	1.23750	0.2475	Prob > F
C. Total	14	160.54400		<.0001*

Figure 6.6: Statistical analysis of Y1 (A), Y2 (B) and Y3(C) for synthesized FePt nanoparticles

Among the selected independent variables affecting atomic composition, X3 demonstrated maximum effect on atomic composition with p value=0.0036followed by X2 (p value=0.0115) and X1 (p value=0.0264) (Figure 6.7). Amongst the interaction between independent variables, the interaction between none of the selected independent variables showed any significant effect on Y2.The full model for effect analysis of critical variables on FePt nanoparticles shows that the factors exert both positive and negative effect on response. In case of Fe%, none of the independent showed negative effect on Y2 but in case of Pt%, X1 and interaction between X1 and X2 demonstrated negative effect on Y2 which means increase in value of X1 alone and X1,X2 in combination will lead to decrease in value of Y3, while X2 alone exerted positive effect on Y3, i.e. increase in X2 will lead to increase in Y3.

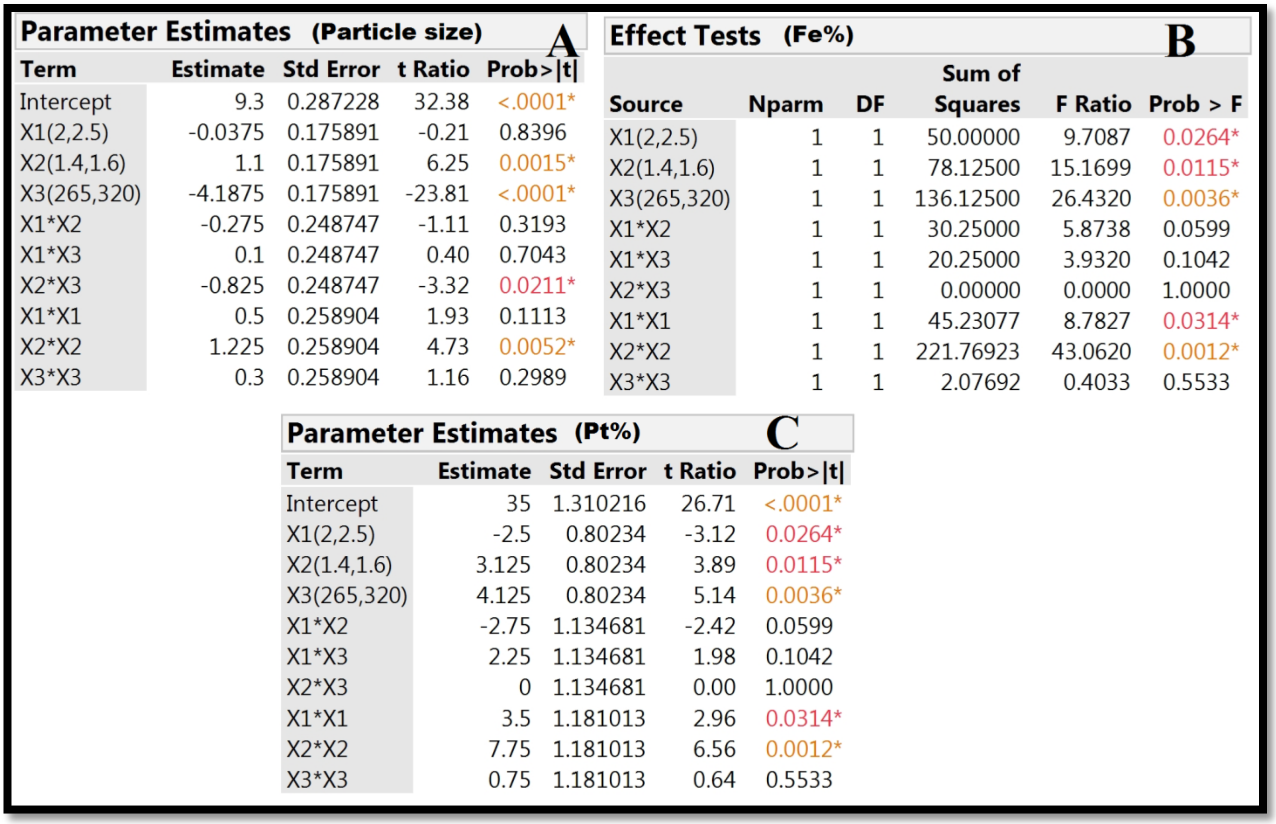

Parameter Estimates (Particle size)

Term	Estimate	Std Error	t Ratio	Prob>|t|
Intercept	9.3	0.287228	32.38	<.0001*
X1(2,2.5)	-0.0375	0.175891	-0.21	0.8396
X2(1.4,1.6)	1.1	0.175891	6.25	0.0015*
X3(265,320)	-4.1875	0.175891	-23.81	<.0001*
X1*X2	-0.275	0.248747	-1.11	0.3193
X1*X3	0.1	0.248747	0.40	0.7043
X2*X3	-0.825	0.248747	-3.32	0.0211*
X1*X1	0.5	0.258904	1.93	0.1113
X2*X2	1.225	0.258904	4.73	0.0052*
X3*X3	0.3	0.258904	1.16	0.2989

Effect Tests (Fe%)

Source	Nparm	DF	Sum of Squares	F Ratio	Prob > F
X1(2,2.5)	1	1	50.00000	9.7087	0.0264*
X2(1.4,1.6)	1	1	78.12500	15.1699	0.0115*
X3(265,320)	1	1	136.12500	26.4320	0.0036*
X1*X2	1	1	30.25000	5.8738	0.0599
X1*X3	1	1	20.25000	3.9320	0.1042
X2*X3	1	1	0.00000	0.0000	1.0000
X1*X1	1	1	45.23077	8.7827	0.0314*
X2*X2	1	1	221.76923	43.0620	0.0012*
X3*X3	1	1	2.07692	0.4033	0.5533

Parameter Estimates (Pt%)

Term	Estimate	Std Error	t Ratio	Prob>|t|
Intercept	35	1.310216	26.71	<.0001*
X1(2,2.5)	-2.5	0.80234	-3.12	0.0264*
X2(1.4,1.6)	3.125	0.80234	3.89	0.0115*
X3(265,320)	4.125	0.80234	5.14	0.0036*
X1*X2	-2.75	1.134681	-2.42	0.0599
X1*X3	2.25	1.134681	1.98	0.1042
X2*X3	0	1.134681	0.00	1.0000
X1*X1	3.5	1.181013	2.96	0.0314*
X2*X2	7.75	1.181013	6.56	0.0012*
X3*X3	0.75	1.181013	0.64	0.5533

Figure 6.7: Parameter estimates for Y1 (A), Y2 (B) and Y3 (C) for synthesized FePt nanoparticles

The result of ANOVA proves that the model was significant for effect of selected variables on particle size with p value < 0.05. The obtained results can be observed visually in the contour plots shown in Fig. 6.9. Contour plots are 2D graphical representation of response against selected factors. We can observe in contour plot between X1 and X3 (Fig. 6.8B) that with increase in X1, no significant variation in Y2 or Y3 was observed which is in accordance with effect analysis of variables on Y2, Y3 and effect model obtained from design. In case of X3, a slight variation in Y2 and Y3 was observed. In plot between X2 and X3 (Fig. 6.8C), we can observe an increase in particle size can be observed with increase in value of X2. In case of X3, homogeneity in atomic composition was observed with increase in value of X3. The contour plot between X1 and X2(Fig. 6.8A) shows that although the effect of X1 was not significant on Y1, at X2 value less than 2.1, slight variation in Y2 and Y3 was observed.

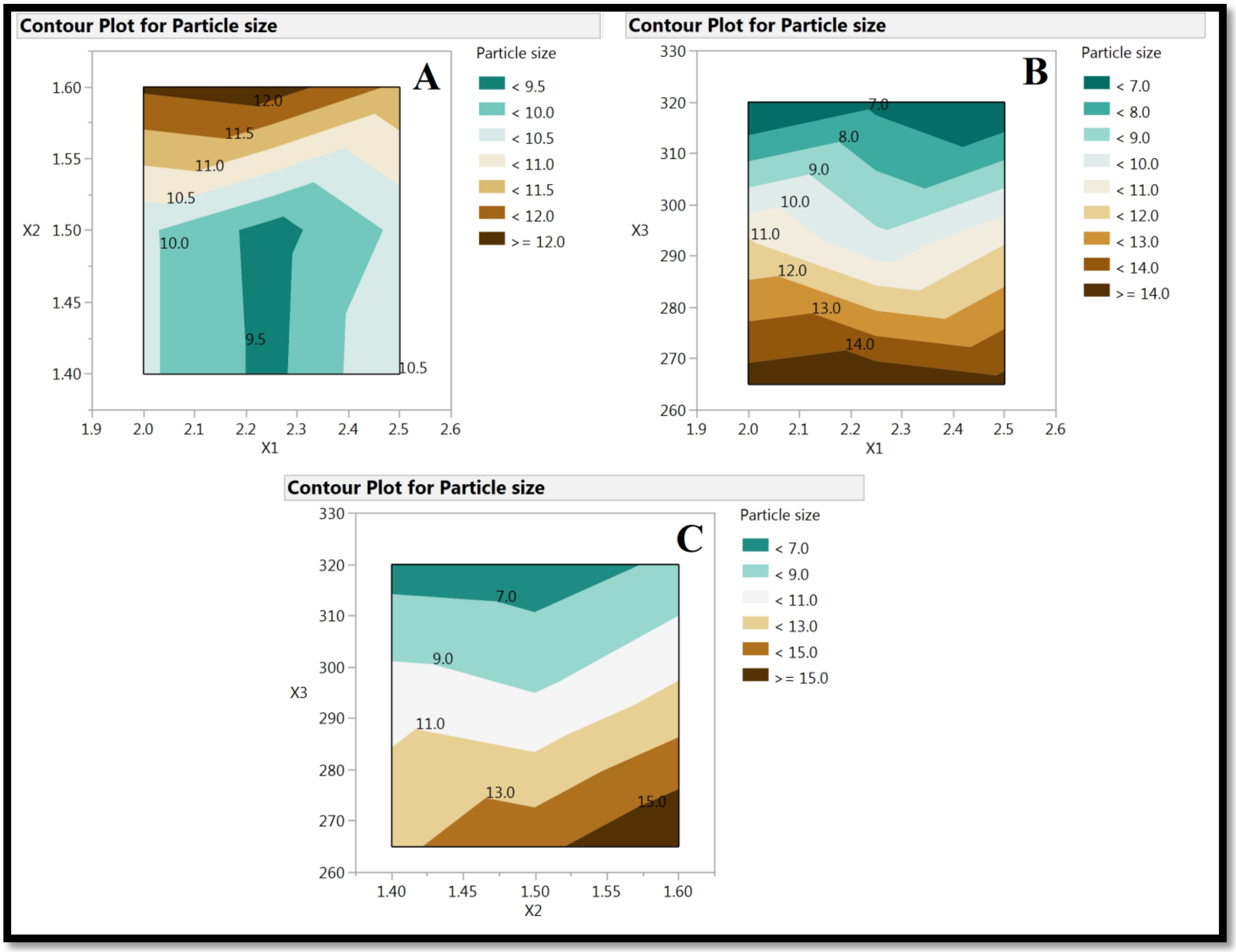

Figure 6.8: Contour plots showing (A) effect of X2 and X1 on Y1; (B) effect of X3 and X1 on Y1; (C) effect of X3 and X2 on Y1for synthesized FePt nanoparticles

As Y2 and Y3 were correlated, the contour plots for Y3 was just opposite of Y2. The effect which leads to decrease in value of Y2 alternatively increased value of Y3.

Desirability plot was generated using SAS JMP software. The upper and lower desired values of response were selected and software generated values of variables which would help to achieve the desired response.

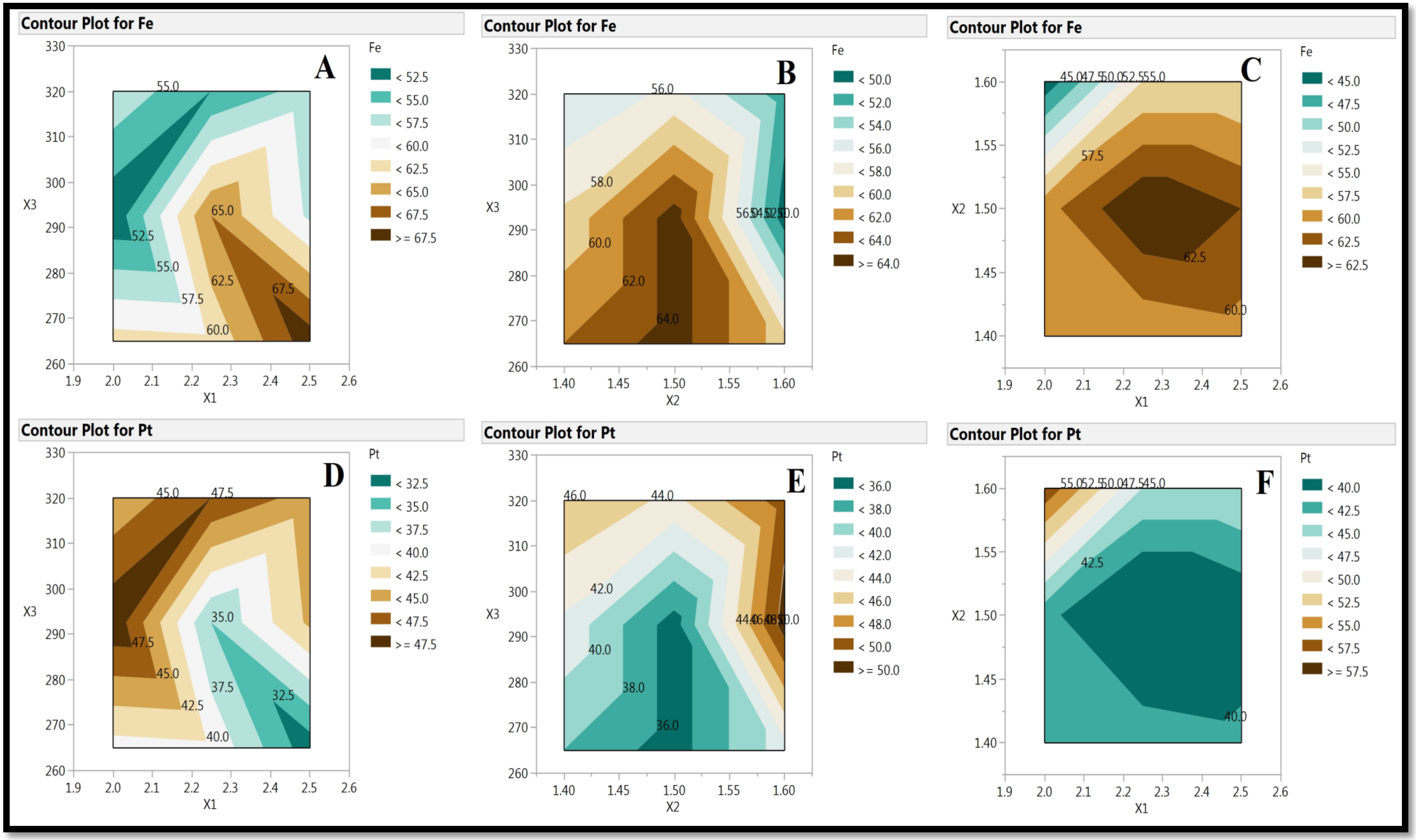

Figure 6.9: Contour plots showing effect of (A) X3 and X1 on atomic percent of Fe (Iron); (B) X3 and X2 on atomic percent of Fe; (C)X2 and X1 on atomic percent of Fe; (D)X3 and X1 on atomic percent of Pt (Platinum); (E) X3 and X1 on atomic percent of Pt; (F) X3 and X1 on atomic percent of Pt in synthesized FePt nanoparticles

The desirability plot is shown in Fig. 6.10. A composite desirability of 0.945 was obtained which predicts that if the nanoparticles are synthesized according to the obtained values of variables, the chance to obtain desired value of response is 94.5%.

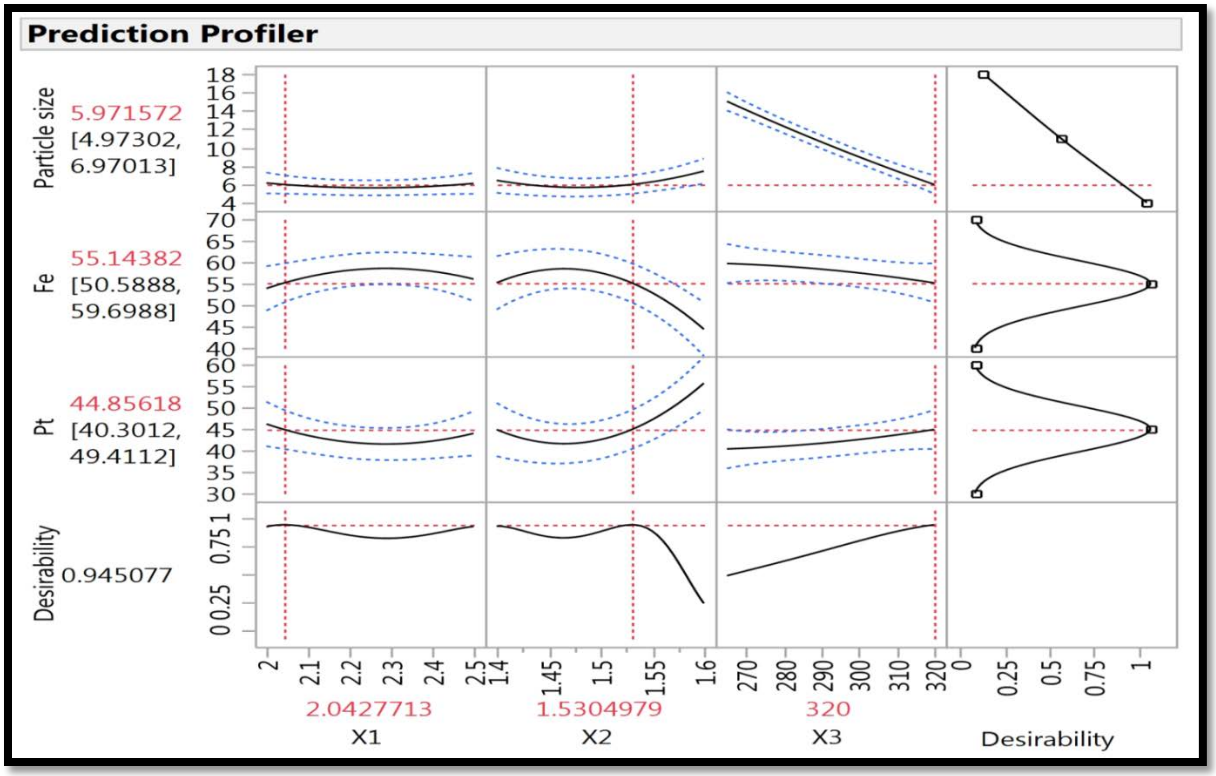

Figure 6.10**:** Desirability plot obtained for synthesis of FePt nanoparticles

The suitability of desirability plot was assessed by synthesizing nanoparticles of suggested batch and comparing it with predicted response (Table 6.4).

Table 6.4**:** Predicted and obtained value for desirability plot for synthesized FePt nanoparticles

Independent variables	**Values**	
X1(Fe:Pt precursor ratio)	2.04 mmol	
X2(Conc. of 1, 2-hexadecanediol)	1.53 mmol	
X3(Reflux temperature)	320°C	
Response	**Predicted**	**Obtained**
Particle size (nm)	5.97	5.7±1.1
% Fe	55.15	52.8
% Pt	44.85	47.2

The obtained results demonstrate the suitability of predicted desirability plot for optimized formulation. Compiled effect of factors on %Fe and particle size of synthesized FePt nanoarticles is shown in Fig 6.11 and 6.12.

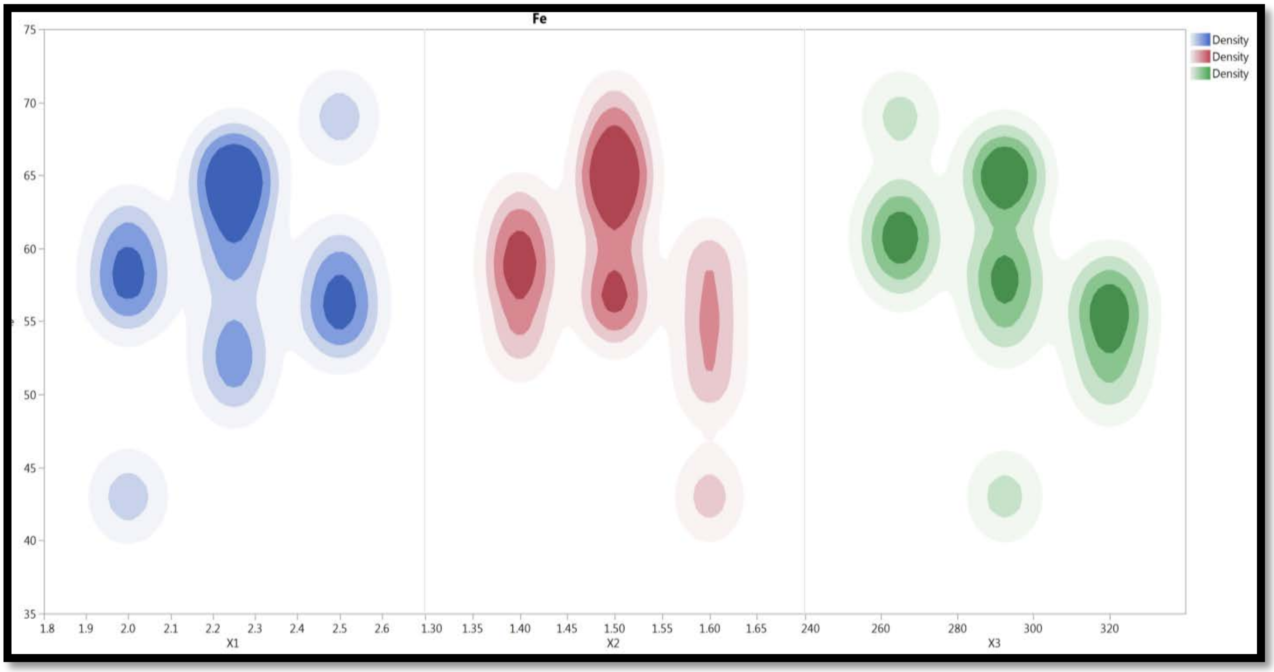

Figure 6.11: Effect of factors on % Fe in FePt nanoparticles

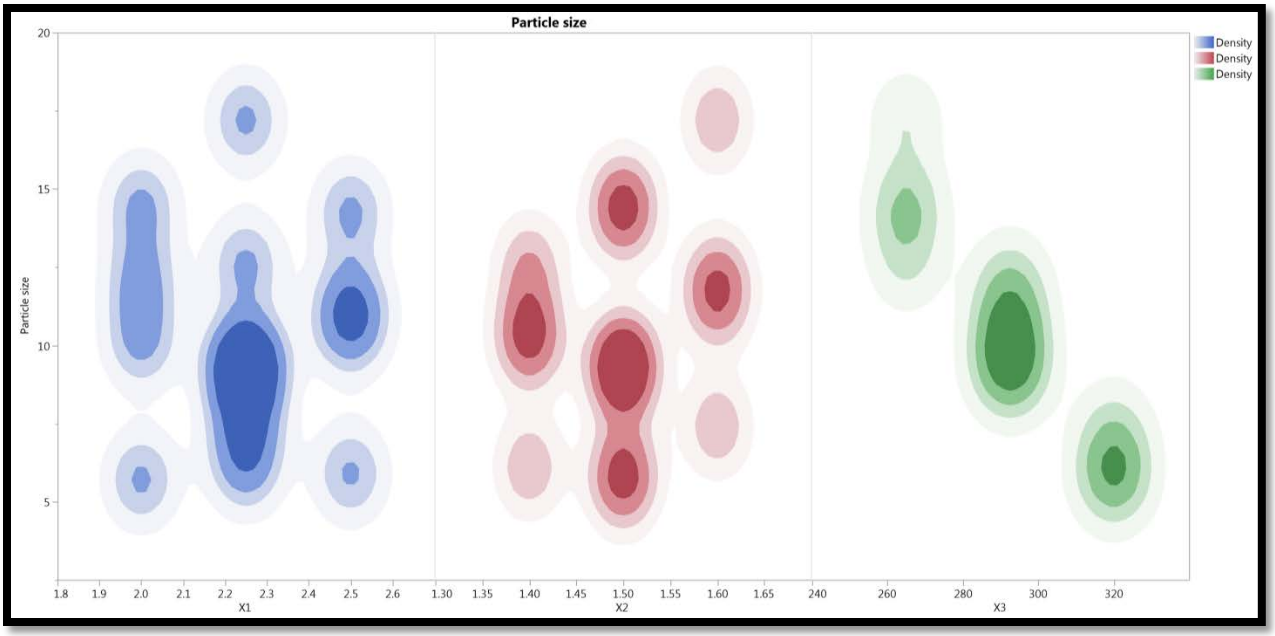

Figure 6.12: Effect of factors on particle size of FePt nanoparticles

6.1.4. Establishment and analysis of design space

Design space" is the space within which the quality of the product can be built. A broad and wider design space leads to a more robust and flexible process for minimizing variation and getting closer to the predicted QAs. ICH Q8 (2008) defines "design space" as "multidimensional combination and interaction of input variables and process parameters that have been demonstrated to provide assurance of quality" [10]. An overlay plot provides a range within which variations in the value of critical variables will not affect the final response and helps in visual examination of the design space [11]. An overlay plot provides a range within which variations in the value of a CPP will not affect the final response (in the present case, the final product QAs). An overlay plot was plotted between the significant critical variables affecting the product QAs (particle size, atomic composition) that were identified after the optimization phase. The composite desirability function based on the set constraints was used to determine the conditions that would result in an optimal formulation design. An overlay plot provides a range within which variations in the value of critical variables will not affect the final response. An overlay plot was plotted between the significant critical variables affecting the desired product response (particle size, atomic composition). Overlay plot was obtained from SAS JMP software by putting the constraints with respect to higher and lower desired values of responses.

Analysis of established design space is very necessary from the scale up point of view. During manufacturing process, there is variation in values of process parameter depending on manufacturing equipment. The design must be robust enough to cope up with these variations such that the final product quality is not affected. It is very important to check and analyze if obtained design space holds correct and the area upper and lower to establish design space yields response which is undesired [12]. With respect to above consideration, analysis of design space was done by plotting overlay plot using Minitab 16 with response upper and lower to established design space. The result obtained after 5% variation in the optimized value demonstrated no significant variation with the variation if any arising being less than 1% (Table 6.4). The percent variation observed in response of DoE created with factors having value with 5% variation from that of optimized formulation is less than 1% suggesting that the design is robust enough to withstand up to 5% variation in CPP (critical process parameter) without having a significant effect on final product quality attribute.

Table 6.5: Effect of variation in CPP on particle size and atomic composition of FePt nanoparticles

Variation (%)	Particle size (nm)	Fe (%)	Pt (%)
5	6.1±1.3	53.2±3.7	47.7±5.2
10	7.6±1.9	57.6±4.8	42.4±3.3

A DoE created with 10% variation in CPP (Table 6.5) gave a variation of more than 5% in the value of obtained response suggesting that a variation of less than 10% in values of CPP will give a product with desired quality attribute. The final range of variables that can give a successful prediction of final quality attribute of product is shown in Table 6.6.

Table 6.6: Final operating range of factors for synthesis of FePt nanoparticles

Sr. No.	Reaction condition	Operating range
1	Molar ratio of precursors (Fe:Pt)	1.94-2.14
2	Oleic acid: Oleylamine	1:0.75-1.2:1 mmol
3	1,2-Hexadecanediol	1.46-1.6 mmol
4	Reflux temperature	304-336^{o}C
5	Reflux time	45 in

6.2. Phase transfer of oleic acid coated FePt NP

Phase transfer of oleic acid coated FePt nanoparticles was carried out to impart hydrophilic nature to synthesized FePt nanoparticles. The separation of oleic acid coated FePt nanoparticles was done using centrifugation because presence of large ferromagnetic FePt nanoparticles in the sample at this stage of the synthesis might result in low yield of the FePt nanoparticles if separation was done using a permanent magnet (instead of centrifugation) [13]. After extraction, the phase transfer of oleic acid coated FePt nanoparticles was done using base assisted bath sonication method. The phase transfer of hydrophobic nanoparticles to hydrophilic phase may be explained as per roll up mechanism. The hydrophobic tails ‘burrow’ into the oleic acid leaving the hydrophilic heads to face the surrounding water which results in the formation of a ball-like structure (a micelle) [14]. After this the non-polar part which in present case is oleic acid is held inside the ball and suspended in water, to be washed away (Figure 6.13).

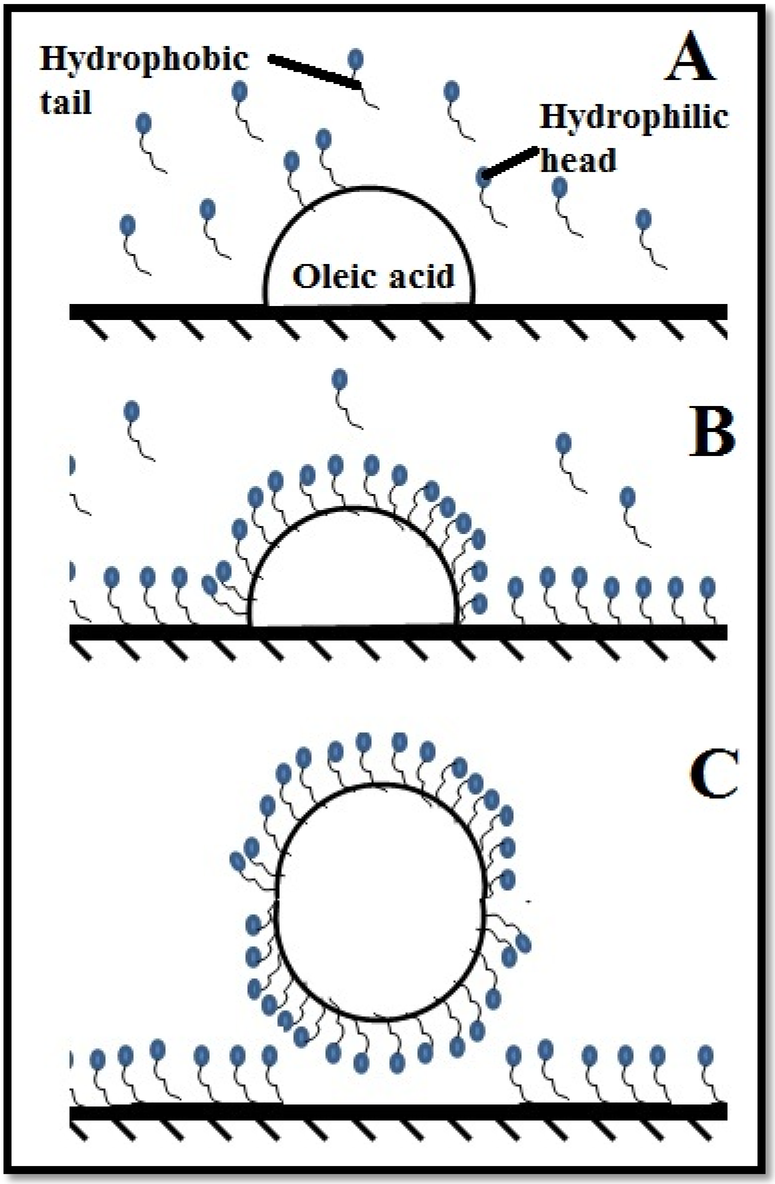

Figure 6.13**:** Mechanism of phase transfer of hydrophobic FePt nanoparticles to hydrophilic phase. (A) adsorption of hydrophobic tail of surfactant on oleic acid; (B) Surface covering of oleic acid; (C) formation of roll up ball of oleic acid covered by surfactant molecules.

Usually this method requires 24 h for complete phase conversion but the time was reduced by occasional probe sonication. The method was optimized to achieve maximum yield (Table 6.7)

Table 6.7: Optimization of Phase transfer condition and process for FePt nanoparticles

Sr. No	**Washing Solution (Water+2-Propanol+KOH)**	**Sonication Time (min)**	**Probe Sonication (min)**	**Stirring Time (h)**	**Yield (%)**
1	10 mL+10 mL+1g	30	1 min-1 cycles	18	43.2±2.9
2	10 mL+15 mL+1g	30	1 min-1 cycles	18	44.7±2.7
3	10 mL+15 mL+1.5g	30	1 min-1 cycles	18	47.3±2.9
5	20 mL+10 mL+1.5g	30	1 min-1 cycles	18	51.4±2.7
6	10 mL+10 mL+1g	60	1 min-2 cycles	12	46.9±2.8
7	10 mL+15 mL+1g	60	1 min-2 cycles	12	53.7±3.7
8	10 mL+15 mL+1.5g	60	1 min-2 cycles	12	58.4±3.8
10	20 mL+10 mL+1.5g	60	1 min-2 cycles	12	59.2±4.1
11	10 mL+10 mL+1g	30	1 min-3 cycles	12	57.6±4.2
12	10 mL+15 mL+1g	30	1 min-3 cycles	12	59.5±3.9
13	10 mL+15 mL+1.5g	30	1 min-3 cycles	12	63.7±3.5
15	20 mL+10 mL+1.5g	30	1 min-3 cycles	12	72.5±3.5
16	10 mL+10 mL+1g	60	1 min-3 cycles	6	57.4±3.9
17	10 mL+15 mL+1g	60	1 min-3 cycles	6	61.2±4.3
19	10 mL+15 mL+1.5g	60	1 min-3 cycles	6	71.8±4.5
20	20 mL+10 mL+1.5g	60	1 min-3 cycles	6	76.4±4.9

Based on optimization data, a washing solution composed ofWater (20 mL), 2-Propanol (10 mL) and KOH (1.5g) was selected for phase transfer while the process condition was set as 60 min initial ultrasonication along with 1 min-3 cycles of probe sonication after each 2h of continuous stirring for 6h.The yield of phase transformed FePt nanoparticles (calculated using eq.) was found to be around 78.1±4.4 using optimized process.

$$\% \, Yield = \left(\frac{W_f}{W_i}\right) * 100 \ldots\ldots\ldots\ldots\ldots\ldots\ldots\ldots \text{Eq.1}$$

Where, W_f= amount of nanoparticles in aqueous phase; W_i= total amount of nanoparticles taken

FT-IR analysis was done to confirm the phase transfer of FePt nanoparticles from hydrophobic phase to hydrophilic phase by desorption of oleic acid from surface of FePt nanoparticles.

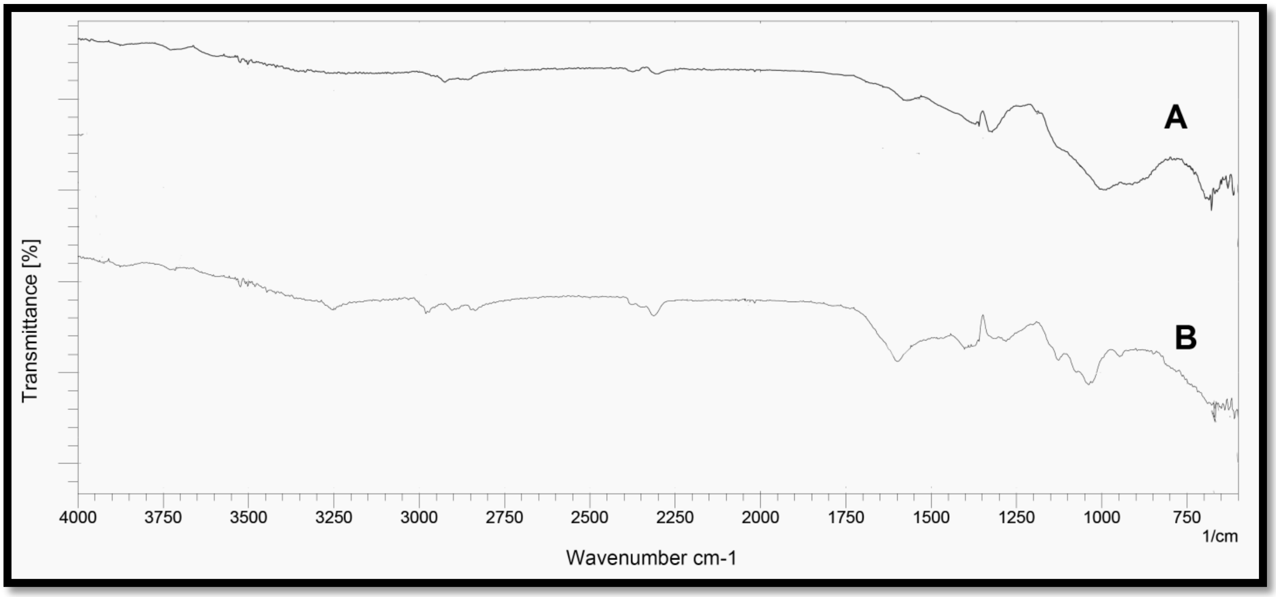

Figure 6.14: FT-IR graph for (A) oleic acid coated and (B) uncoated FePt nanoparticles

The phase transfer of oleic acid coated FePt nanoparticles (A) is also evident by FT-IR spectroscopy (Figure 6.14). The oleic acid coated FePt nanoparticles showed peak of CH_2 bands at around 2900, 2850, and 1460 cm^{-1}. Above mentioned bands are characteristic for the CH_2 chains present in oleic acid. The presence of oleic acid was further confirmed by presence of alkene stretchings at 3058, 2990, and 1680 cm^{-1}, CH_3 stretchings at 2950 and 2880 cm^{-1}, and carboxylate stretchings at 1540 and 1410 cm^{-1} [15]. This presence of carboxylate stretchings at 1540 and 1410 cm^{-1} provides the idea that oleic acid is chemisorbed onto the FePt nanoparticles' surface via its carboxylate group through a bidentate bond rather than a monodentate bond [16]. The strong IR band at 585 cm-1 is characteristic of the Fe-O vibrations related to the ferrite core [17]. The Peak at 2065-2070 cm-^{1} confirmed presence of Pt in the sample [17]. Most of these peaks of oleic acid were not observed in case of phase transferred FePt nanoparticles (B) confirming phase transfer of FePt nanoparticles.

6.3. Surface modification of FePt Nanoparticles

6.3.1. Grafting of amine groups on FePt NP Using APTES (NH_2-FePt)

Silanization with organo-functional alkoxysilane molecules are generally used to functionalize FePt nanoparticles with amine groups (NH_2-FePt). 3-Aminopropyltriethoxysilane (APTES) is commonly used to prepare cationic amine groups on nanoparticles [18]. This system offers only one functional group for chemical conjugation with targeting ligands or fluorescent tags. This was the first step towards formation of bi-functional FePt nanoparticles. The amine functionalization was later confirmed by FT-IR spectroscopy. The FT-IR results (Figure 6.15) confirms the grafting of amine groups on the surface of FePt nanoparticles. The successful grafting of silane group is evidenced by presence of two broad bands at 3430 and 1615 cm^{-1} in the FT-IR spectrum of Fe_2O_3-NH_2, which are attributed to the N–H stretching vibration and N–H bending respectively [19]. The symmetric and the asymmetric CH_2 stretching modes peaks can be observed at 2928 and 2830 cm^{-1} respectively. The peak for Fe–O–Si bonds was not observed due to spectrum overlapping at 590 $cm^{-1}$with the Fe–O vibrations of magnetite [20]. The presence of silane layer on the surface of nanoparticles was confirmed by the presence of band at 1128 cm^{-1} corresponding to the Si–O–Si bond [21]. The estimation of elemental composition and amine functional groups of FePt-NH_2 was done using EDAX and TGA (Table 6.7). The total carbon content of unmodified FePt nanoparticles was found to be 0.2% which can be attributed to surface adsorbed CO_2 and oleic acid. The carbon content of FePt-NH_2 nanoparticles increased from 0.2% to 1.31% due to silane group i.e. 1.29% increase in carbon content**.** Density of FePt nanoparticles (having average hydrodynamic size ~ 5.8 nm), was calculated using method reported by Svedberg et al., $d_p = \left(\frac{\sqrt{18\eta_s s}}{\rho_p - \rho_s}\right)$, (where, d_p=d_H=hydrodynamic diameter of FePt nanoparticles, ρ_p=solvent density, ρ_s=density of nanoparticle, s= sedimentation coefficient of solute) and was found to be approximately 4.35 g cm^{-3}. The number of amino groups on each FePt-NH_2 nanoparticles was estimated using the formula $N = (\omega N_A \rho \frac{4}{3} \Pi r^3 * 10^{-23})/MM$, where, *N* is the number of ligands on each particle, *R* is the mean radius of the FePt nanoparticles (5.8 nm), ρ is the density of the nanoparticles (4.35 g/cm^3), *N*A is Avogadro's number, *MM* is the molar mass of the ligand molecules (g/mol) and $\omega$is the mass loss in percent (%) calculated using TGA. The free amino group in synthesized Fe_2O_3-NH_2 was estimated using fluorescamine assay [22]. Initially, 0.5 mL of fluorescamine was added to PLL solution at various concentrations. The reaction mixture was incubated at room temperature for 10 min followed by recording of emission spectrum under a 392 nm excitation. Background fluorescence was measured using distilled water alone. For estimation of amino groups in Fe_2O_3-NH_2, 0.5 mL of fluorescamine was added to Fe_2O_3-NH_2dispersion and incubated for 10 min followed by emission recording under a 392 nm excitation. The average number of amine group was found to be ~ 95 amine molecule on each nanoparticle (Table 6.8). In case of amine modified FePt using PEI, the average number of amino group (147) was more than those modified using APTES (Table 6.8**)**. This can be attributed to the fact that PEI has higher number of amine groups compared to APTES owing to its branched nature which provides large number of amine groups on similar surface area of nanoparticles [23]. The carbon content of FePt-NH_2 nanoparticles increased from 0.2% to 2.16% due to silane group i.e. 1.96% increase in carbon content which is due to surface adsorbed PEI. The details of PEI modified FePt nanoparticles are shown in Table 6.8.

Table 6.8**:** Characterization of FePt, FePt-$NH_2$and NH_2-FePt-COOH nanoparticles

Sr. No	**Nanoparticles**	**Particle size (nm)**	**Zeta Potential**	**% carbon content**	**No. of free amine group**
1	FePt	5.8±0.8	13±1.1	0.23%±0.05%	0
2	FePt-NH_2(APTES modified)	6.0±0.9	29±1.4	1.52%± 0.47%	95±3
3	FePt-NH_2(PEI modified)	6.2±0.8	37±1.9	2.16%±0.25%	147±7
4	NH_2-FePt-COOH (APTES modified)	6.2±0.9	21±1.4	1.61%±0.34%	71±5
5	NH_2-FePt-COOH (PEI modified)	6.5±1.1	29±1.3	2.47%±0.28%	119±3

Post modification of FePt-NH_2 was done with COOH group by reaction of surface-bound amine groups of FePt-NH_2 with succinic anhydride and was named as B-FePt (bi-functional FePt nanoparticles; NH_2-FePt-COOH). The successful modification of amine group was evidenced and qualitatively monitored by FT-IR (Figure 6.15). The presence of free carboxylic group was observed by the characteristic C=O stretching absorption peak at 1728 cm^{-1} in the spectrum of B-FePt nanoparticles. The C=O stretching band along with the N–H bending band of amide linkage can be observed at 1645 cm^{-1} and 1568 cm^{-1} [23]. The elemental composition of B-FePt was quantified using EDAX and TGA. The carbon content of B-FePt nanoparticles increased from 1.52% (as estimated in FePt-NH_2) for APTES modified and 1.61% for PEI modified to 2.16% for APTES modified while 2.47% for PEI modified due to post-functionalization with COOH group. The increase in carbon content after COOH functionalization confirms partial conversion (due to reaction with succinic anhydride) of amine groups present on FePt-NH_2 nanoparticles into COOH groups. This partial conversion of amine group to carboxylic group imparts dual functionality to B-FePt nanoparticles and is advantageous for tagging two types of functional species reacting with the two distinct –NH_2 and –COOH functionalities. No significant change in the particle size of FePt nanoparticles was observed after chemical modification with APTES and succinic anhydride.

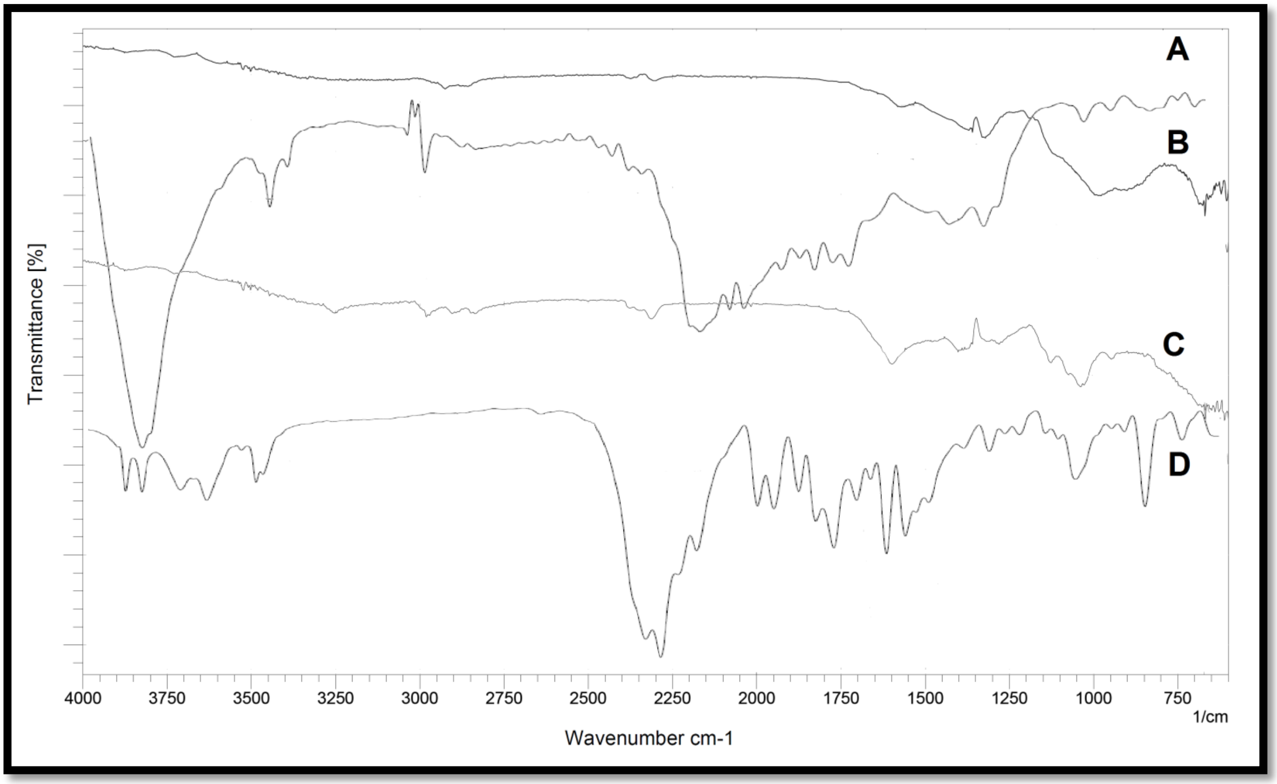

Figure 6.15: FT-IR spectra of unmodified FePt nanoparticles (A), amine modified FePt nanoparticles (B), oleic acid coated FePt nanoparticles (C), and B-FePt nanoparticles (D).

The variations in surface potential of FePt nanoparticles after surface functionalization are shown in Table 6.7**.** The variation in surface potential can be attributed to the presence of functional group on the nanoparticles. In case of unmodified FePt nanoparticles, the surface potential was found to be 13±1.1 mV. On surface modification with APTES, the surface potential shifts towards positive side (29±1.4mV). The shifting of surface potential on positive size was more evident in PEI modified FePt nanoparticles. This increase is attributed to presence of multiple amine functional groups on PEI which is not the case with APTES. On post modification with succinic anhydride, decrease in surface potential was observed. The decrease was more pronounced in case of NH_2-FePt-COOH (PEI modified) compared to NH_2-FePt-COOH (APTES modified) because of excess amine groups present on PEI which are available for reaction with succinic anhydride. XRD analysis was performed to analyze the arrangement of molecules in FePt nanoparticles. X-ray diffraction analysis (Figure 6.16) showed the strongest peaks of the (111) and the (200) facet of a face-centered cubic (fcc) structure [24]. The broad XRD patterns suggested smaller particle size which was in accordance with particle size obtained in TEM analysis and zetasizer [25].

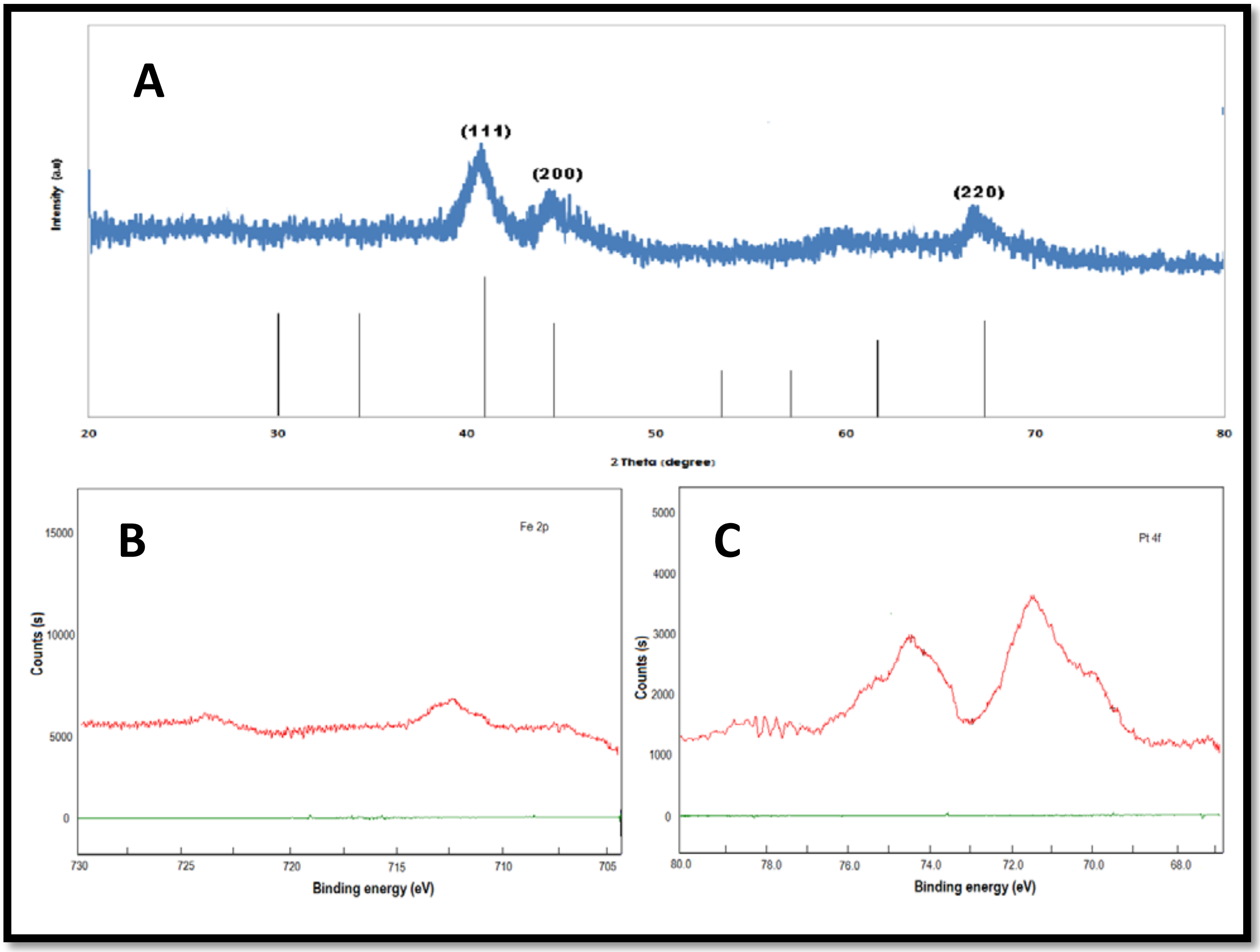

Figure 6.16**:** Characterization of FePt nanoparticles using (A) XRD; (B) XPS analysis of Fe in FePt nanoparticles; (C) XPS analysis of Pt in FePt nanoparticles

The EDAX analysis (Figure 6.17) of the FePt samples revealed the presence of Fe, Pt, nitrogen, and carbon. The presence of nitrogen was only observed in FePt-NH_2, while carbon was observed in all FePt nanoparticles although the composition content was variable (Table 6.9). The chemical states of Fe and Pt elements in FePt nanoparticles were detected using XPS **(**Figure 6.15 (B,C**)**. The signal for both Pt and Fe was split into two spin orbit doublet. The Pt 4f signal for Pt element split into 4f7/2 and 4f5/2 with maxima at around 71.0-71.5 eV and 74.0-75.0 eV respectively. The Fe 2p signal also split into 2p3/2 and 2p1/2 with maxima observed at around 710.5-711.5 eV and 724-725 eV due to spin-orbit coupling [26-28].

Table 6.9: Elemental composition of FePt, FePt-NH_2 and COOH-FePt-NH_2 nanoparticles

Nanoparticles	**Carbon (%)**	**Nitrogen (%)**	**Iron (%)**	**Platinum (%)**	**Oxygen (%)**
FePt	0.23±0.05	0.14±0.05	52.43±2.7	47.05±2.9	0.15±0.02
FePt-NH_2	2.16±0.25	0.87±0.07	51.17±3.1	45.61±3.2	0.19±0.01
COOH-FePt-NH_2	2.47±0.28	0.82±0.04	50.13±3.4	45.14±3.2	1.44±0.06

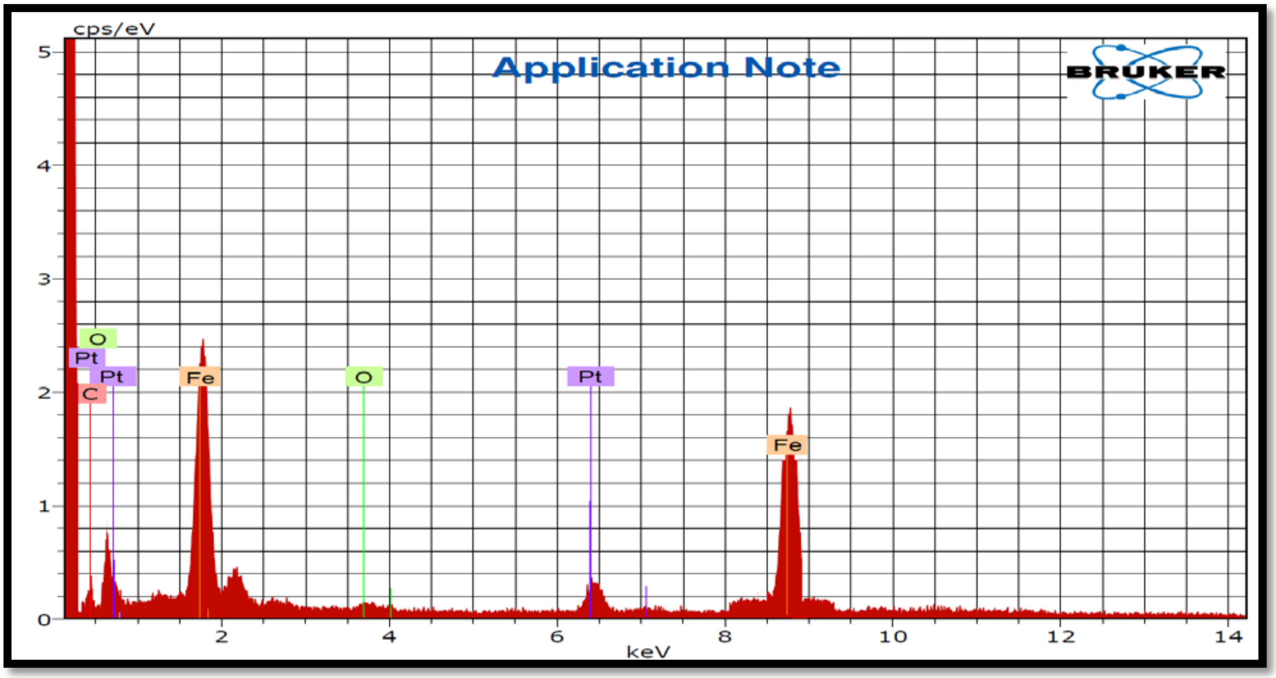

Figure 6.17**:** EDAX of FePt-NH_2 nanoparticles

The thiol modified FePt nanoparticles (SH-FePt) and COOH modified FePt nanoparticles (FePt-COOH) using Poly(acrylic acid) (PAA) was not selected for further characterization studies as the yield of FePt-SH was very low and became unstable after 3h (Table 6.10) While, FePt-COOH using PAA formed semi solid with gel like consistency after phase transfer. Hence, these two nanoparticles were excluded from further characterization studies.

Table 6.10**:** Stability study of SH-FePt and FePt-COOH (synthesized using PAA)

Sr. No.	Nanoparticles	Particle size (nm)		Zeta potential	Yield	Remark
		Initial	After 3h			
1	FePt-SH	6.2±0.6	13.9±1.8	-13.2±1.1	21%±2.2%	Low yield
2	FePt-COOH	6.5±0.9	NA	-21.4±1.6	NA	Unstable

6.4. Synthesis of Fe_2O_3@FePt Nanoparticles

FePt nanoparticle hold promising potential for tumor therapy but it has limitation of low hyperthermia generation and ROS generation as both of these phenomenons depend on the iron content in nanoparticles. Keeping above factor in mind, synthesis of Fe_2O_3@FePt nanoparticles was done using previously reported method [26].Fe_2O_3@FePt nanoparticles owing to high iron content possess both advantage of FePt nanoparticles and Fe_2O_3nanoparticles. The observed particle size of synthesized Fe_2O_3@FePt nanoparticles was 8.3±1.3nm. The slight increase in particle size of Fe_2O_3@FePt as compared to FePt nanoparticles is attributed to deposition of Fe_2O_3 over FePt core. The synthesized nanoparticles were then characterized. The optimization data for Fe_2O_3@FePt nanoparticles is shown in Table.6.11. The synthesis method involves single step (one pot synthesis) similar to FePt nanoparticles. The only variables were the molar ratio of Fe and Pt precursor, reaction temperature and reaction time.

Table 6.11**:** Optimization data for synthesis of Fe_2O_3@FePt nanoparticles

Sr. No.	**Molar ratio of Pt:Fe precursor**	**Temperature (^{0}C)**	**Particle size (nm)**	**Atomic composition (Fe:Pt) (%)**
1	1:1.25	200	15.2±1.5	37:63±3.9
2	1: 1.25	240	11.9±2.1	44:56±5.2
3	1: 1.25	280	8.9±2.1	49:51±4.8
4	1: 1.25	300	9.7±1.1	52:48±4.2
5	1:1.25	280	8.8±1.4	49:51±2.4
6	1:1.5	280	8.5±1.5	53:47±2.5
7	1:1.75	280	8.9±1.9	57:43±3.1
8	1:2	280	8.6±1.5	66:34±2.1
9	1:2	270	8.7±1.2	64:36±3.6
10	1:2	260	8.5±1.3	64:36±3.5
11	1:2	250	8.3±1.3	60:40±2.8

At lower temperature, the obtained particle size was larger and atomic composition of Fe_2O_3@FePt nanoparticle was not uniform. At higher temperature, decrease in particle size was observed similar to that of FePt nanoparticles. Initially, reaction temperature was optimized (based on particle size and atomic composition) by keeping molar ratio of Pt and Fe constant (1:1.25) and increasing reaction temperature from 200 ^{0}C to 300 ^{0}C. Next, the molar ratio of Pt and Fe precursor was optimized by keeping temperature constant at 280 ^{0}C and changing molar ratio from 1:1.25 to 1:2. The Fe_2O_3@FePt nanoparticle with desired particle size and atomic composition was obtained at molar ratio of 1:2 for Pt and Fe precursor (Table 6.11).The atomic composition of Fe_2O_3@FePt nanoparticle obtained at molar ratio of 1:2 (Pt:Fe) keeping temperature 280 ^{0}C was slightly more than desired ratio (Fe:Pt) of 60:40. Hence, reaction temperature was decreased to 250 ^{0}C keeping molar ratio of precursor constant. The obtained Fe:Pt atomic composition was 60:40 and hence was selected as optimum reaction condition for synthesis of Fe_2O_3@FePt nanoparticles.

6.5. Surface modification of Fe_2O_3@FePt Nanoparticles

Various ligands were used for modifying surface of synthesized Fe_2O_3@FePt nanoparticles such as SH, COOH, NH_2, HA, TPP, LND, FITC, DOTA-NH_2, DOTA-NCS and Ctx. The surface modification of Fe_2O_3@FePt nanoparticles was done with the aim of imparting tumor targeting ability and cellular co-localization specificity to nanoparticles for efficient treatment of tumor. The surface modification using various surface functionalities was assessed using FT-IR, particle size and zeta potential (Table 6.12).

Table 6.12**:** Particle size and zeta potential of surface modified nanoparticles

Sr. No.	**Surface modified nanoparticles**	**Particle size (nm)**	**Zeta potential (mV)**
1	Fe_2O_3@FePt	8.3±1.3	-19.7±2.1
2	Fe_2O_3@FePt-SH	8.7±1.2	-23.6±2.7
3	Fe_2O_3@FePt-COOH	8.7±1.2	-33.7±2.5
4	Fe_2O_3@FePt-NH_2 (using PEI)	9.1±1.1	21.5±2.9
6	Fe_2O_3@FePt-NH_2-HA	11.4±1.3	12.7±2.6
7	Fe_2O_3@FePt-NH_2-FITC	9.3±1.1	-11.2±1.9
8	Fe_2O_3@FePt-NH_2/COOH	9.1±1.2	-12.8±2.1
9	Fe_2O_3@FePt-NH_2-TPP	11.2±1.3	45.6±2.9
10	Fe_2O_3@FePt-NH_2-TPP-COOH	11.7±1.5	38.4±2.7
11	Fe_2O_3@FePt-NH_2-TPP-COOH-Ctx	14.5±1.8	43.7±3.1
12	Fe_2O_3@FePt-NH_2/COOH-Drug	19.7±1.7	25.7±2.4
13	Fe_2O_3@FePt-NH_2-TPP-COOH-Drug	22.3±1.6	38.3±2.4
14	Fe_2O_3@FePt-COOH-DOTA-NH_2	15.1±1.3	29.7±2.5
15	Fe_2O_3@FePt-NH_2-DOTA-NCS	14.8±1.1	31.5±3.2
16	Fe_2O_3@FePt-NH_2/COOH-TPP-Drug-HA-Ctx	27.4±2.1	35.1±2.9
17	Fe_2O_3@FePt-NH_2/COOH-TPP-Drug-HA-Ctx (pH sensitive)	29.6±1.9	37.2±1.7

The particle size of surface modified Fe_2O_3@FePt nanoparticles was more or less similar without any significant difference. Non-significant change in particle size of Fe_2O_3@FePt, Fe_2O_3@FePt-

SH, Fe_2O_3@FePt-COOH, Fe_2O_3@FePt-NH_2, Fe_2O_3@FePt-NH_2-FITC and Fe_2O_3@FePt-NH_2/COOH nanoparticles is due to the fact that the surface modifying functional group hardly varies the size of Fe_2O_3@FePt nanoparticles. In case of other surface modified Fe_2O_3@FePt nanoparticles, significant increase in size was observed in comparison to unmodified Fe_2O_3@FePt nanoparticles as the surface modifying agents were having atomic size large enough to vary the particle size of nanoparticles [27].There was variation in observed zeta potential which can be attributed to presence of different functional groups on surface of nanoparticles.

The various modifications were done for improving the targeting ability of nanoparticles to tumor cell as well as cellular co-localization of nanoparticles after cellular uptake. The modifications were done with specific aim. The conjugation of Ctx was done so as to provide the nanoparticles ability to target hypoxic tumor cells while TPP modification was done to impart mitochondrial targeting ability to Fe_2O_3@FePt nanoparticles. The surface modification with DOTA was done with the aim of radiolabeling Fe_2O_3@FePt nanoparticles for radiotherapy as well as imaging purpose. The conjugation of FITC was done for studying cellular uptake and cellular co-localization in cell lines along with and distribution of Fe_2O_3@FePt nanoparticles after *in vivo* administration. Based on the desired quality attributes of Fe_2O_3@FePt nanoparticles, few amongst the various surface modified Fe_2O_3@FePt nanoparticles were selected for further study viz. Fe_2O_3@FePt-NH_2/COOH-TPP-Drug-HA-Ctx, Fe_2O_3@FePt-NH_2-TPP-COOH-Drug, Fe_2O_3@FePt-NH_2-COOH-Drug and Fe_2O_3@FePt-NH_2-DOTA-NCS nanoparticles.

6.5.1. Characterization of Synthesized Nanoparticles

The characterization of both FePt and Fe_2O_3@FePt nanoparticles was done using various techniques. Particle size and zeta potential was analyzed using Malvern zetasizer and value is shown in Table6.11. X-ray diffraction analysis of FePt and Fe_2O_3@FePt nanoparticles (Figure 6.18) showed the strongest peaks of the (111) and the (200) facet of a face-centered cubic (FCC) structure [28]. Broader XRD patterns obtained for FePt nanoparticles suggest smaller particle size which was in accordance with particle size obtained in TEM analysis (Figure 6.20) and zetasizer. The EDAX analysis (Figure 6.19) of the FePt and Fe_2O_3@FePt revealed the presence of Fe, Pt, nitrogen, and carbon. The chemical states of Fe and Pt elements in FePt nanoparticles were detected using XPS **(**Figure 6.21**)**. The signal for both Pt and Fe was split into two spin orbit doublet. The Pt 4f signal for Pt element split into 4f7/2 and 4f5/2 with maxima at around 71.0-71.5 eV and 74.0-75.0 eV respectively [29]. The Fe 2p signal also split into 2p3/2 and 2p1/2 with maxima observed at around 710.5-711.5 eV and 724-725 eV due to spin-orbit coupling [30]. Similarly, for Fe_2O_3@FePt, same signal was obtained for Pt and Fe along with another signal at 710 eV which is attributed to presence of Fe^{+2}over FePt core.AFM images show spherical shape of FePt and Fe_2O_3@FePt nanoparticles with smooth surface (Figure 6.22). The AFM images show that particle size of FePt nanoparticles was around 6nm while that of Fe_2O_3@FePt nanoparticles was 9.4 nm which is similar to that obtained by particle size analyzer and TEM analysis. AFM under scanning mode shows smooth spherically shaped Fe_2O_3@FePt nanoparticleswhich confirm uniform layering of Fe_2O_3 over FePt nanoparticles also visible in STEM (scanning transmission electron microscopy) of Fe_2O_3@FePt nanoparticles (Figure 6.20) over FePt nanoparticles which make it more responsive to magnetic field. The magnetic hysteresis loop is shown in Figure 6.23.

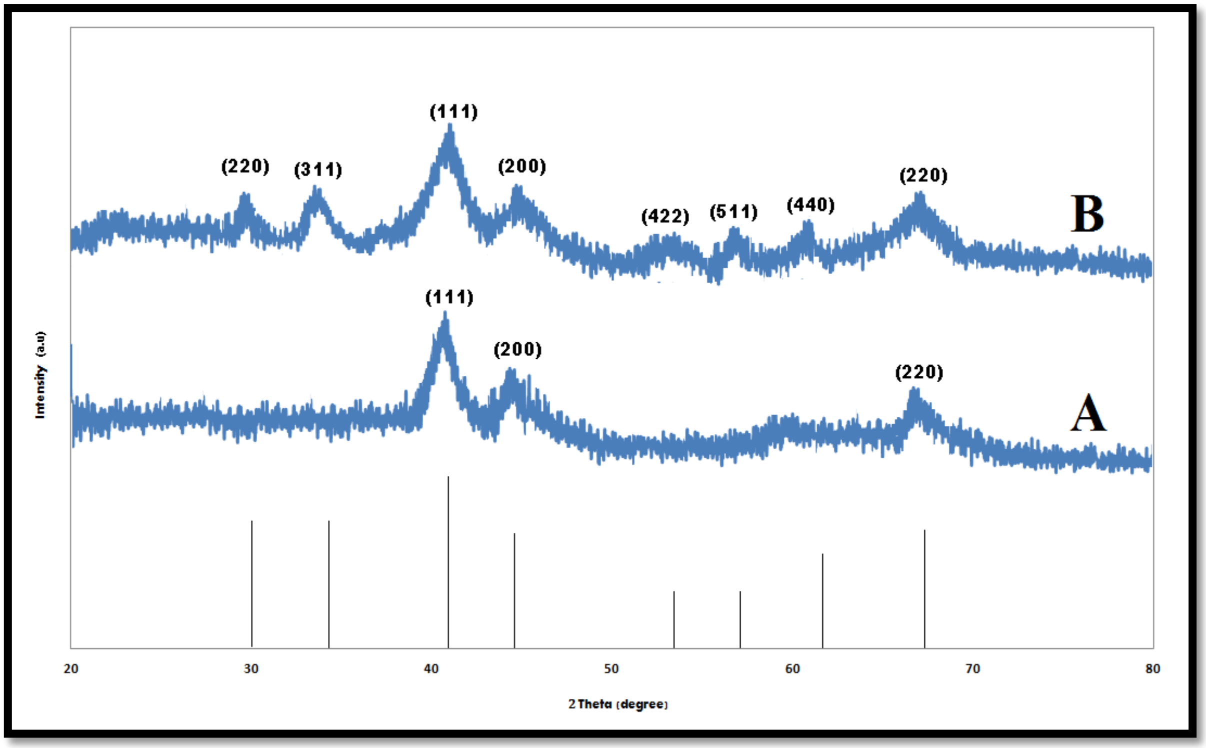

Figure 6.18: XRD peaks of (A) FePt and (B) Fe_2O_3@FePt nanoparticles

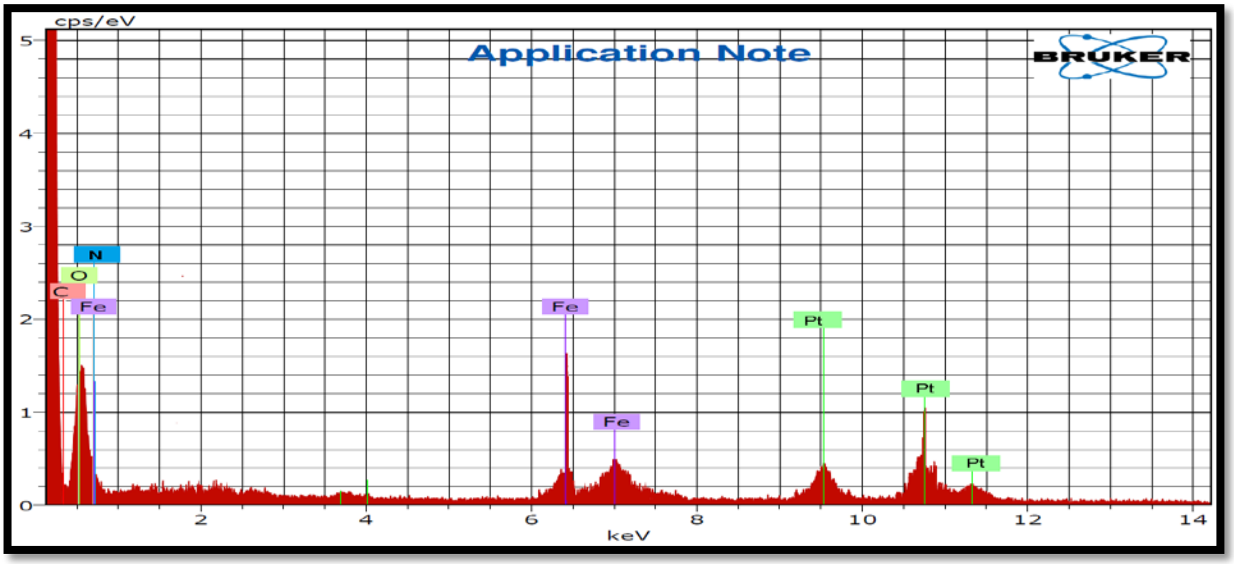

Figure 6.19: EDAX of Fe_2O_3@FePt nanoparticles

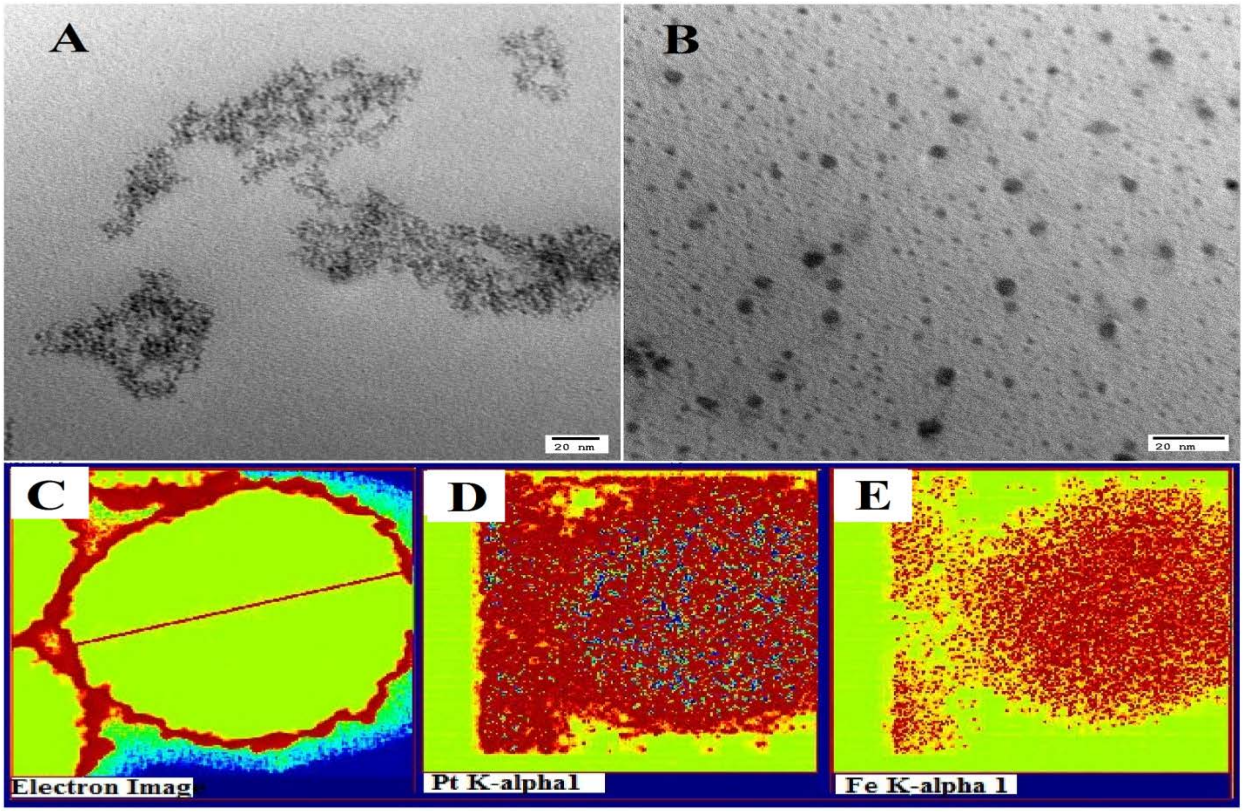

Figure 6.20: TEM of (A) FePt and (B) Fe_2O_3@FePt nanoparticles; STEM image of (C) Fe_2O_3@FePt nanoparticles showing presence of Fe_2O_3over FePt nanoparticles; (D) Pt in Fe_2O_3@FePt nanoparticles (blue dots);(E) Fe (red dots) in Fe_2O_3@FePt nanoparticles.

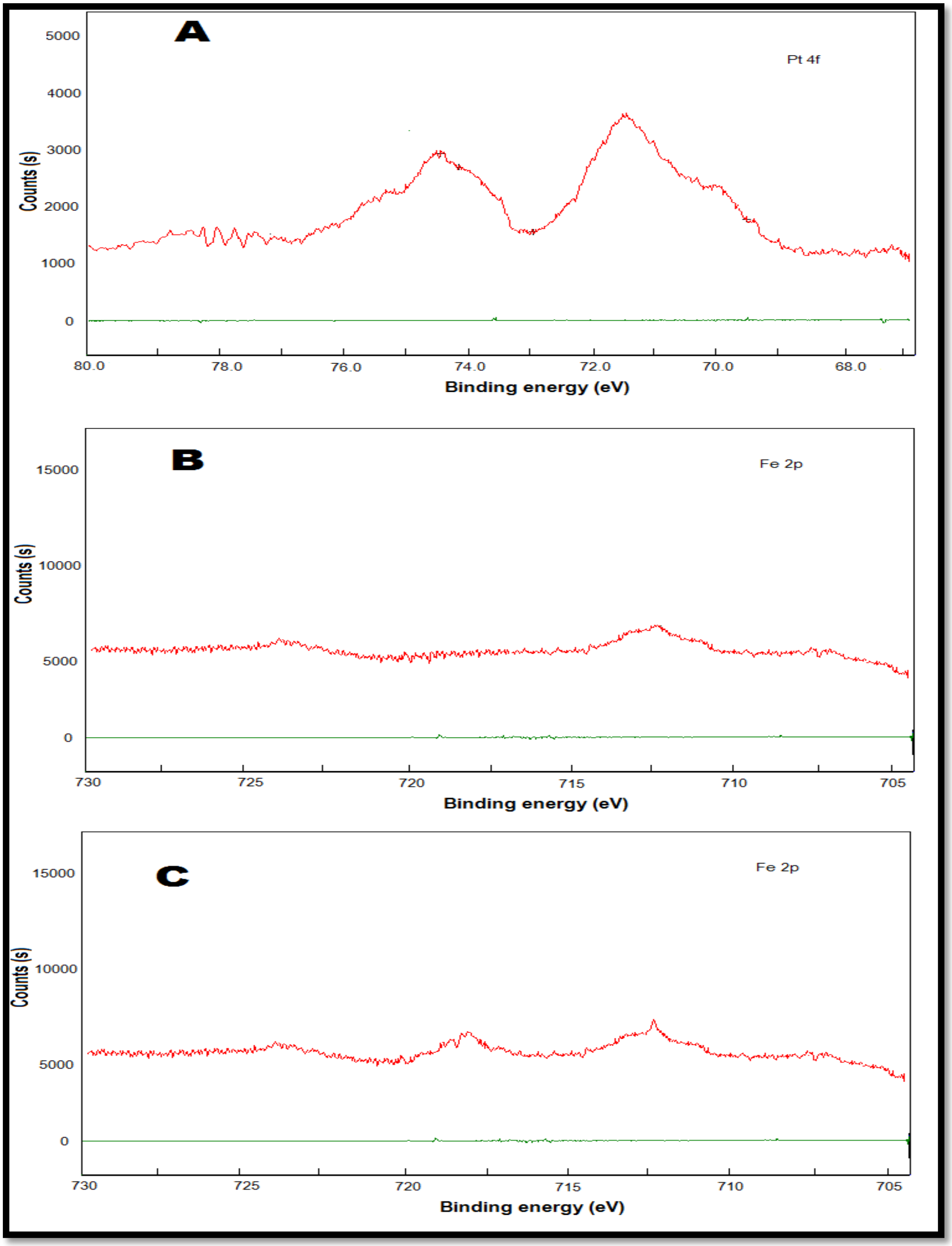

Figure 6.21: XPS of Fe_2O_3@FePt nanoparticles; (A) Pt 4f of FePt core; (B) Fe 2p of FePt core; (C) Fe 2p of Fe_2O_3 shell.

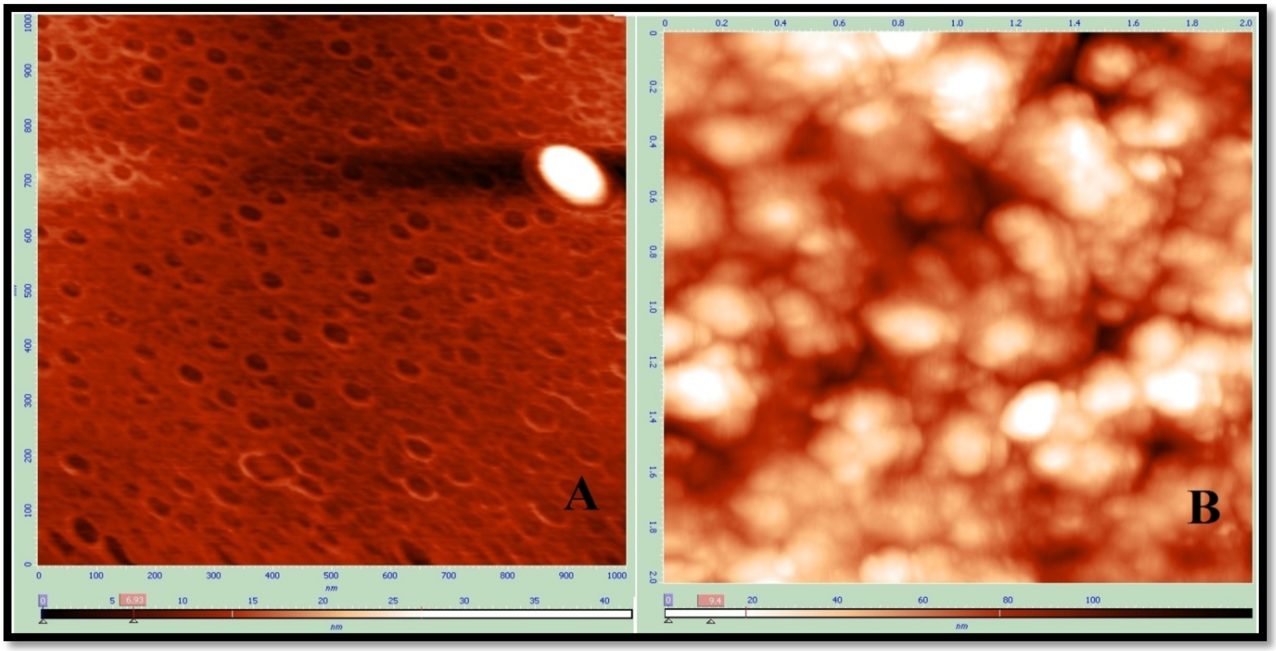

Figure 6.22: AFM images of (A) FePt (6.43nm); (B) Fe_2O_3@FePt (9.4nm) nanoparticles

The magnetic behaviour of FePt nanoparticles and Fe_2O_3@FePt nanoparticles was studied using VSM (vibrating sample magnetometer). The FePt nanoparticles exhibited a superparamagnetic state with low remnant magnetization at room temperature along with low value of magnetic saturation (Hs).The magnetic behavior obtained in case of Fe_2O_3@FePt was better than FePt nanoparticles which are due to presence of iron oxide layer [31].

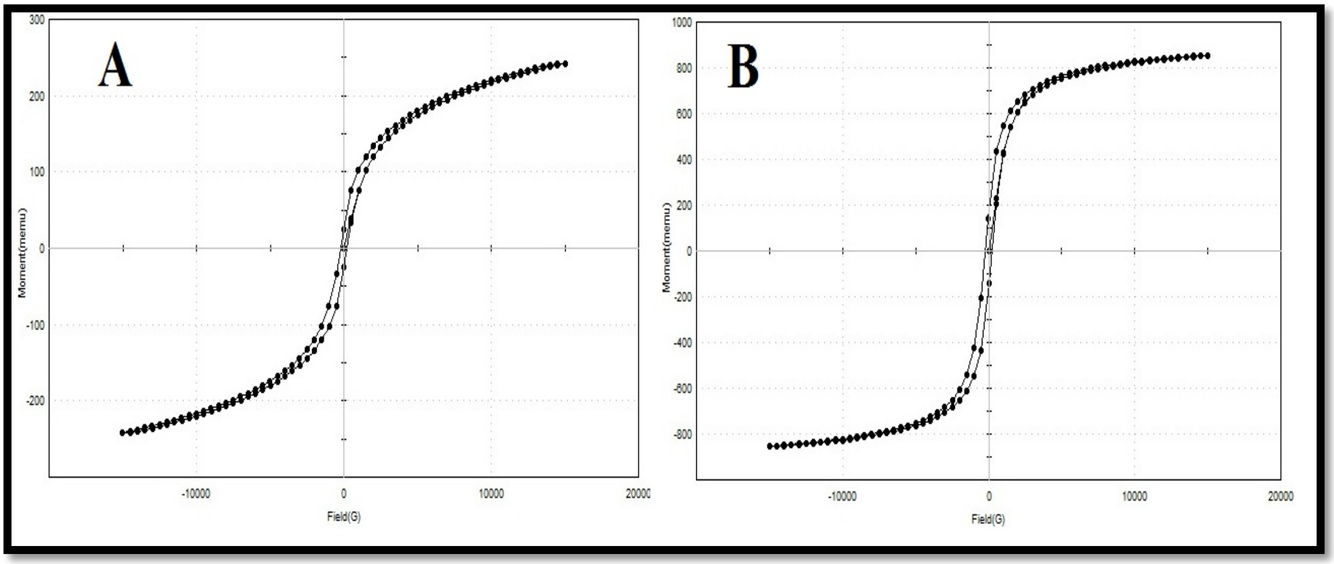

Figure 6.23: Magnetic hysteresis of curve of (A) FePt and (B) Fe_2O_3@FePt nanoparticles

We can observe from the magnetic hysteresis curve that the saturation magnetic moment for FePt nanoparticles was around 250 emu while for Fe_2O_3@FePt nanoparticles, it was around 900 emu. The enhancement in magnetic saturation magnetization of Fe_2O_3@FePt nanoparticles was due to presence of Fe_2O_3 layer over FePt nanoparticles. This enhanced effect is responsible for higher hyperthermia generation by Fe_2O_3@FePt nanoparticles in comparison to FePt nanoparticles [32]. Apart from hyperthermia generation, the high saturation magnetization will be helpful for enhancing MR contrast behavior of Fe_2O_3@FePt nanoparticles along with magnetically controlled movement of Fe_2O_3@FePt nanoparticles under externally controlled magnetic field [33, 34]. FePt and Fe_2O_3@FePt nanoparticles were also characterized using Raman spectroscopy. The Raman spectra clearly showed (Figure 6.24) presence of carboneous material on surface of FePt and Fe_2O_3@FePt nanoparticles. Two bands centered around 1400 cm^{-1} and 1600 cm^{-1} for all the annealed samples. These bands have been identified as the D band and G band, respectively, which occur for graphitic carbon which can be attributed to formation of carbon layer due to pyrolysis of oleic acid at higher temperature [35].

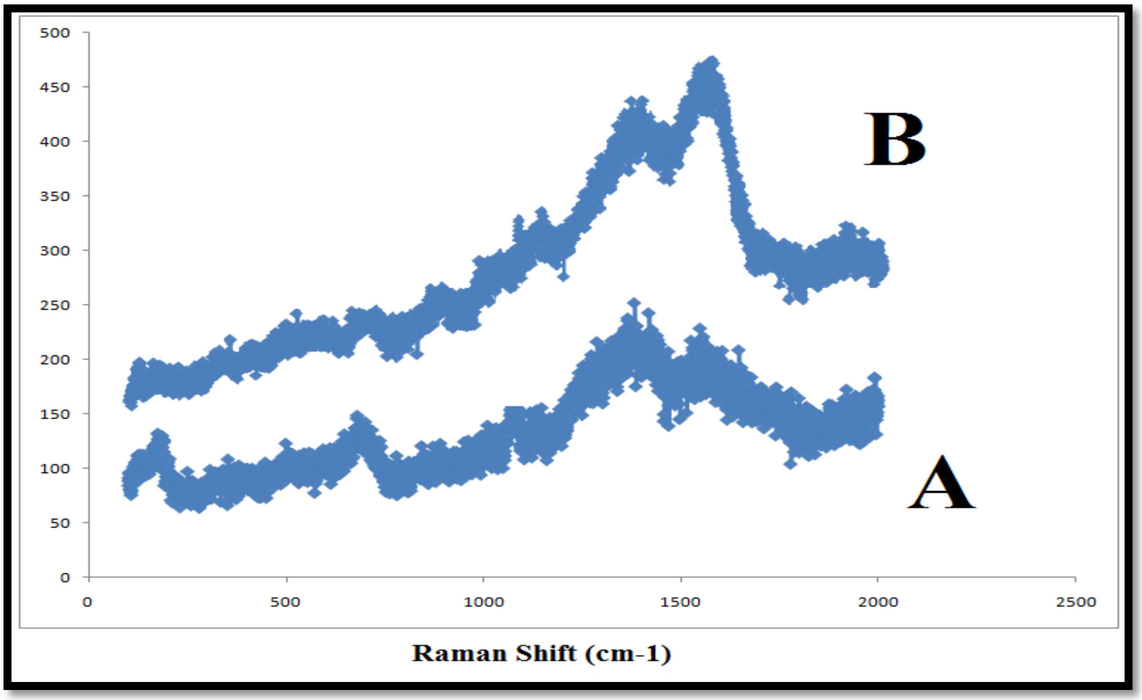

Figure 6.24: Raman shift for (A) FePt nanoparticles; (B) Fe_2O_3@FePt nanoparticles.

6.6. *In vitro* Magnetic Hyperthermia (NIR triggered Hyperthermia (Photothermal) and Dual Magnetophotothermal Measurement)

In vitro dual heating of FePt and Fe_2O_3@FePt nanoparticles was studied in PBS suspension and U87MG (glioblastomas) cells. The cells were first incubated for 4 h with FePt nanoparticles with varying concentration (2.5-20mg). The FePt and Fe_2O_3@FePt nanoparticles suspension and cells loaded with FePt and Fe_2O_3@FePt nanoparticles were subjected to five different heating protocols: (i) magnetic hyperthermia alone at167.6 Oe, 251.4 Oe and 335.2 Oe; (ii) photothermia alone with 808 nm laser at power range 0.8 W/cm^2 and 2.5 W/cm^2; (iii) photothermia alone with 1064 nm laser at power range 0.8 W/cm^2 and 2.5 W/cm^2; (iv) combined hyperthermia with 808 nm laser at power range 0.8 W/cm^2 and 2.5 W/cm^2 with magnetic hyperthermia at 335.2 Oe; (v) combined hyperthermia with 1064 nm laser at power range 0.8 W/cm^2 and 2.5 W/cm^2 with magnetic hyperthermia at 335.2 Oe [36].Samples were placed in the heating coils(copper) of induction heating unit (Easy Heat 8310, Ambrell; UK)and temperature was recorded at the bottom of the sample. Figure 6.24 (for FePt) and 6.25 (for Fe_2O_3@FePt) shows temperature profile obtained with each protocol.

The increase in hyperthermia generated with increase in concentration can be attributed to the fact that the efficiency of the magnetic induction heating depends on the following parameters like: 1) magnetic nanoparticles properties as size, distribution and surface functionality 2) concentration and volume of fluid 3) duration and strength of applied magnetic field [37]. At any particular concentration of FePt and Fe_2O_3@FePt nanoparticles, the increase in hyperthermia was proportional to increase in magnetic field strength. From obtained results, we can observe that the increase in temperature with increase in concentration of FePt and Fe_2O_3@FePt nanoparticles at a particular magnetic field strength was proportion alto magnetic field strength to an extent after which the increase was not significant which has been reported previously as dwell temperature [38]. In the finite-size nanoparticle system, the heat generated by magnetic fluids under an AMF is mainly attributed to two contributions: hysteresis loss and N´eel–Brownian relaxation losses. While N´eel relaxation is due to rapidly occurring changes in the direction of magnetic moments relative to the crystal lattice and is hindered by anisotropy energy that tends to orient the magnetic domain in a given direction relative to the crystal lattice, Brownian relaxation is attributed to physical rotation of particles within a medium in which they are placed (external dynamics) and is hindered by the viscosity that tends to counter the movement of particles in the medium [39].

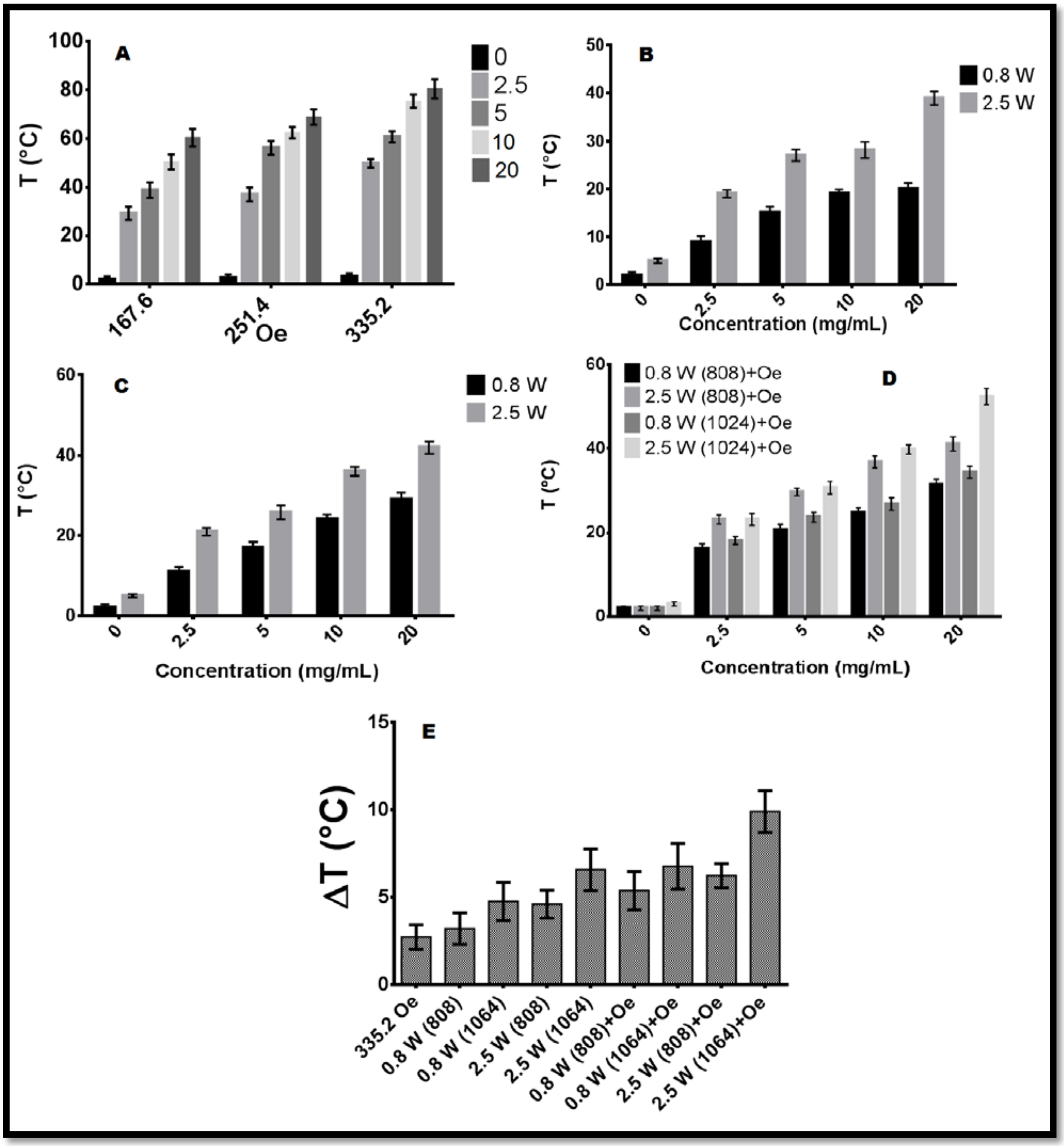

Figure 6.25:*In vitro* generation of heat in FePt nanoparticles suspension in response to applied magnetic field (A), NIR laser treatment (808nm) (B), NIR laser treatment (1064nm) (C), NIR laser treatment+335.2Oe magnetic field (D) and *in vitro* heat generation in presence of applied

magnetic field (335.2 Oe), NIR laser treatment (808 and 1064 nm) and combined magnetic field (335.2 Oe) and NIR laser treatment (808 nm and 1064nm) (E).

Brownian relaxation can play important role in deciding the hyperthermia generated in physiological conditions [40]. The tumor density is more than normal tissue due to high collagen content due to which there is viscosity difference between normal tissue and tumor cells. Time required for reaching hyperthermia temperature (45^o C) which is required for killing cancer cells decreases with increase in magnetic field strength but at same magnetic strength, time required to reach a particular temperature might change with change in surrounding media viscosity owing to change in Brownian relaxation [41]. To study the effect of viscosity on hyperthermia generation by FePt and Fe_2O_3@FePt nanoparticles, SAR (specific absorption rate) variation of FePt and Fe_2O_3@FePt nanoparticles was calculated by mimicking physiological tumor condition. To mimic tumor physiological conditions, FePt and Fe_2O_3@FePt nanoparticles were dispersed in 5% agarose gel, which is used to simulate the in vivo environment of animal tissue phantoms [42]. The obtained results (Table 6.13) showed no significant variation in SAR of FePt and Fe_2O_3@FePt nanoparticles in PBS (358 Wg^{-1}, 412 Wg^{-1}) and 5% agarose gel (325 Wg^{-1}, 361 Wg^{1}). The obtained experimental results confirm that the hyperthermia generated by FePt and Fe_2O_3@FePt nanoparticles in PBS outside body will be similar inside tumor having highly viscous surrounding.

Table 6.13: SAR of FePt and Fe_2O_3@FePt nanoparticles in PBS and 5% agarose gel

Sr. No.	**Condition**	**FePt**	**Fe_2O_3@FePt**
1	PBS	358 Wg^{-1}±23.5 Wg^{-1}	412 Wg^{-1}±34.7 Wg^{-1}
2	5% agarose gel	325 Wg^{-1}±21.7 Wg^{-1}	361 Wg^{1}±31.2 Wg^{-1}

The hyperthermia generated by NIR is directly correlated to NIR optical absorption by nanoparticles [43]. Iron nanoparticles have demonstrated NIR absorption mainly due to charge transfer and ligand transitions of iron. Figure 6.25 and 6.26 shows temperature profile obtained after laser irradiation. The absorbance increased with increase in concentration of FePt and Fe_2O_3@FePt nanoparticles leading to linear increase in temperature. The temperature increase recorded at 1064 nm was higher than 808 nm due to higher absorbance in the NIR second region resulting from Fe^{2+}-Fe^{3+} transition in FePt and Fe_2O_3@FePt nanoparticles [44].

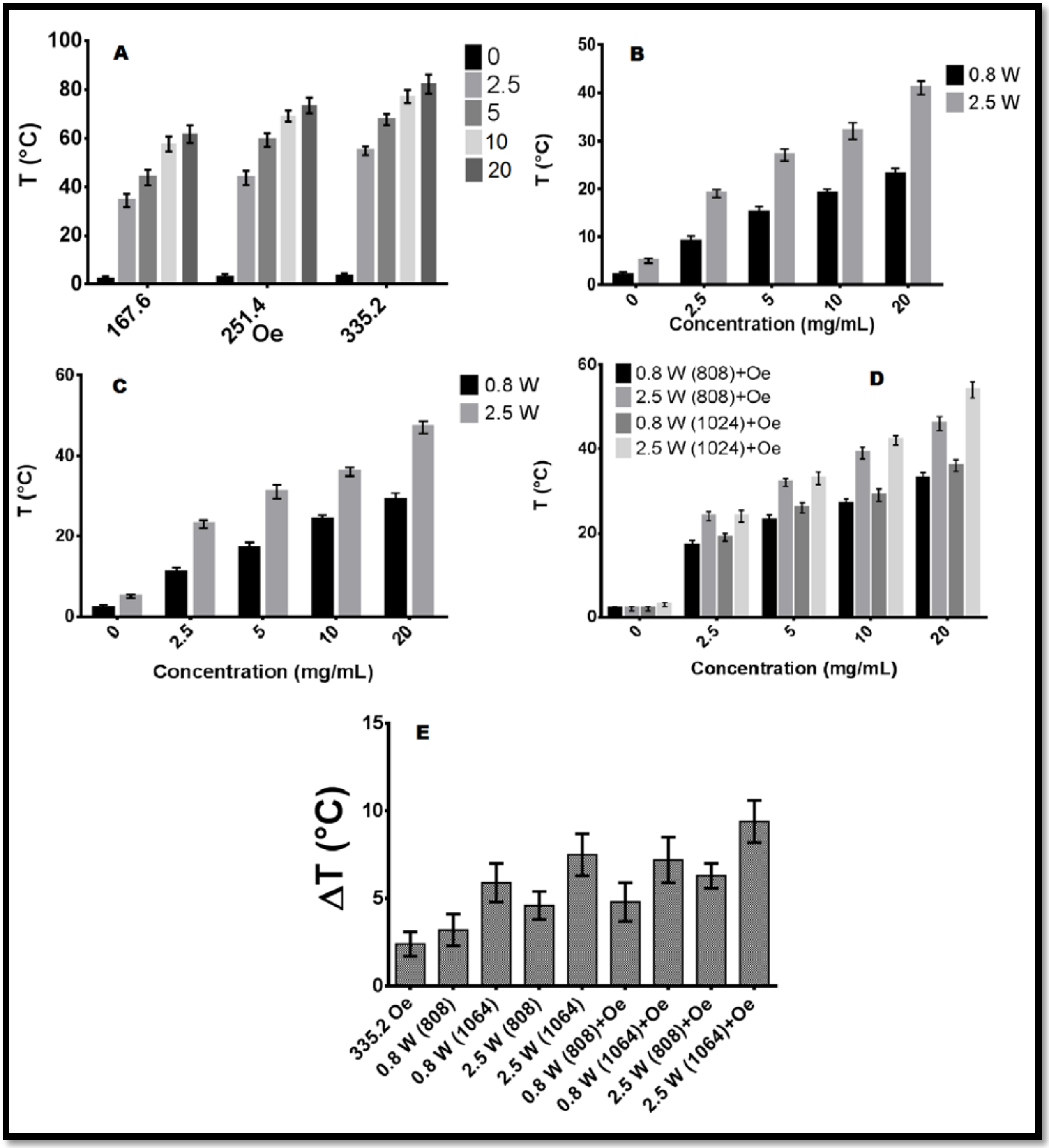

Figure 6.26: *In vitro* generation of heat in Fe_2O_3@FePt nanoparticles suspension in response to applied magnetic field (A), NIR laser treatment (808nm) (B), NIR laser treatment (1064nm) (C), NIR laser treatment+335.2Oe magnetic field (D) and *in vitro* heat generation in presence of

applied magnetic field (335.2 Oe), NIR laser treatment (808 and 1064 nm) and combined magnetic field (335.2 Oe) and NIR laser treatment (808 nm and 1064nm) (E).

It has been reported that magnetic hyperthermia has the advantage of unlimited tissue penetration. The nanoparticles on further laser irradiation exhibit plasmonic resonance towards the NIR region of spectra and hence could penetrate biological tissue such as tumor mass [45]. This was demonstrated by mimicking in vitro tumor mass. To mimic tumor mass, about 15 million FePt and Fe_2O_3@FePt nanoparticles labelled cells were concentrated in a small volume in an Eppendorf (150µL). The tumor cells loaded with FePt and Fe_2O_3@FePt nanoparticles (25mg) were then subjected to above mentioned heating protocol. For heating protocol 1, the observed hyperthermia generated was less than that observed in suspension which may be due to confinement of FePt and Fe_2O_3@FePt nanoparticles in endosomes which was not in case of heating protocol involving laser irradiation. The dual heating mode was synergistic and more efficient compared to lone hyperthermia or laser irradiation. The heating power (specific loss of power (SLP)) of FePt and Fe_2O_3@FePt nanoparticles (Table 6.14**)** in suspension for magnetic hyperthermia (~300-500 W/g)alone was less than that obtained for laser irradiation (~800-1800 W/g) and dual heating mode (~3000-4500 W/g), while in cell line (Table 6.15) magnetic hyperthermia (~180-250 W/g) alone was much less than that obtained for laser irradiation (~600-1500 W/g) and dual heating mode (~2500-3500 W/g).

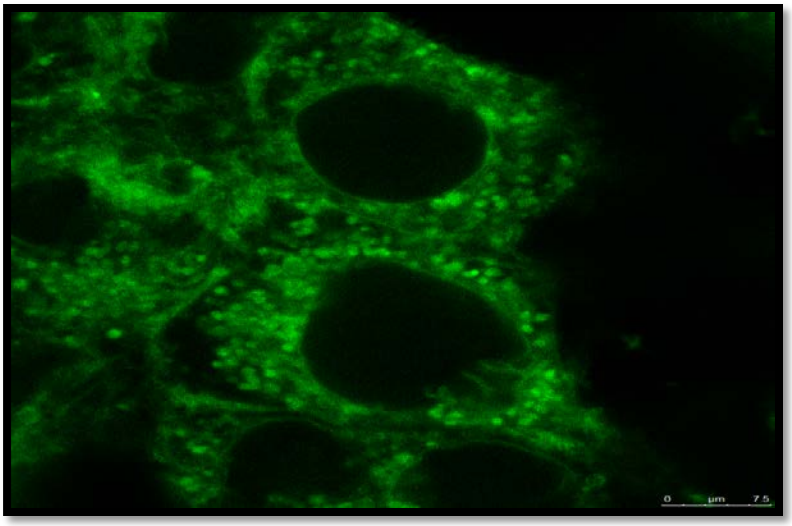

Figure 6.27: Endosomal localization of FePt nanoparticles in U87MG cells

The variation in SLP for magnetic hyperthermia and laser irradiation in cell line and suspension can be attributed to the fact that thermal energy provided by laser irradiation restores the Brownian motion of FePt and Fe_2O_3@FePt nanoparticles in the cellular environment [46]. In case of magnetic hyperthermia, the magnetic relaxation dynamics is governed by Neel relaxation which is inhibited in case of FePt and Fe_2O_3@FePt nanoparticles confined in densely sequestered endosomes (Figure 6.27). This inhibition of magnetic dynamics is absent in case of photothermal heating. The obtained results suggest that both the magnetic hyperthermia and photothermal heating can be tuned by varying the concentration of FePt and Fe_2O_3@FePt nanoparticles, magnetic field strength, laser frequency, laser strength and irradiation time.

Table 6.14**:** Heating power of FePt and Fe_2O_3@FePt nanoparticles suspension

Sr. No.	**Protocol**	**FePt**	**Fe_2O_3@FePt**
1	Magnetic field (335.2Oe)	286±18.5W/g	449±21.4 W/g
2	NIR laser treatment (808nm)	590±37.2 W/g	1350±56.1 W/g
3	NIR laser treatment (1064nm)	1240±51.5 W/g	1830±77.2W/g
4	Combined magnetic field (335.2 Oe) and NIR laser treatment (808 nm and 1064nm)	3350±57.6W/g	4500±55.8 W/g

Table 6.15**:** Heating power of FePt and Fe_2O_3@FePt nanoparticles in U87MG cells.

Sr. No.	**Protocol**	**FePt**	**Fe_2O_3@FePt**
1	Magnetic field (335.2Oe)	182±19.7W/g	248±26.3 W/g
2	NIR laser treatment (808nm)	810±27.9 W/g	970±59.9 W/g
3	NIR laser treatment (1064nm)	1110±56.1 W/g	1530±81.2W/g
4	Combined magnetic field (335.2 Oe) and NIR laser treatment (808 nm and 1064nm)	2560±49.3W/g	3180±54.1 W/g

6.7. Determination of carboxyl modification

The degree of substitution was calculated using the equation6.1 &6.2. [47].

$$n_{COOH} = (V_b - V) * C_{HCl} \quad \text{(Equation 6.1)}$$

Where, n_{COOH}= moles of carboxyl groups

V_b= volume of HCl needed to titrate blank = 4.0

V = volume of HCl needed to titrate sample =3.2

C_{HCl} = conc. of HCl = 0.05

Hence, n_{COOH} was found to be 0.04 M.

$$DS = \frac{MW_{DSU} * n_{COOH}}{m_{dry} - MW_1 * n_{COOH}} \quad \text{(Equation 6.2)}$$

Where, DS = degree of substitution

MW_{DSU} =MW of an unsubstituted disaccharide unit = 161 Da

m_{dry} = mass of dry CMHA = 12.5 mg

MW_1 = increase in MW due to carboxyl group substitution = 58 Da

After putting all the values in equation 6.2, degree of substitution was found to be 0.6325.

The percent carboxyl modification = DS × 100%

So, average % modification was found to be 63.25%.

6.7.4. Infrared Spectroscopy of CMHA

Figure 6.28 & 6.29 shows the IR spectrum of HA & CMHA. The IR spectrum of synthesized CMHA was compared with standard HA spectrum (Table 6.16). The obtained IR spectrum of CMHA showed all characteristic peaks of HA with greater intensity. These changes indicate carboxy-methylation of HA. So, it was confirmed that the CMHA was formed [48].

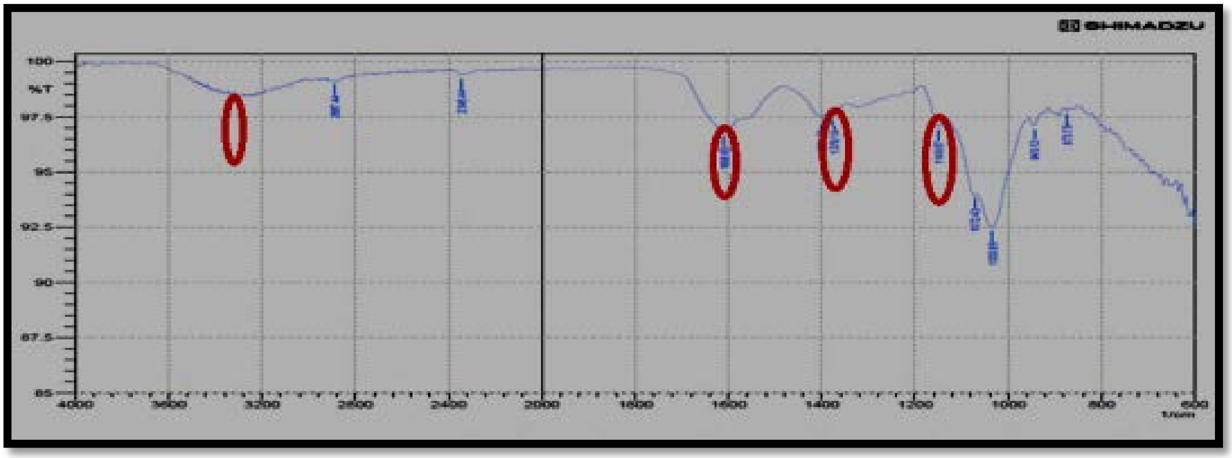

Figure 6.28: FT-IR spectrum of hyaluronic acid

Figure 6.29: FT-IR spectrum of CMHA

Table 6.16: FT-IR spectrum data for HA & CMHA

Observed Frequency(cm^{-1})	**Reported Frequency(cm^{-1})**	**Inference**
3250	3280	O-H,N-H Stretching
2910	2900	C-H Stretching
1598,1394	1600,1410	C-O-C Stretch
1398	1414-1401	$-CH_2COOH$

6.7.5. Nuclear Magnetic Resonance (NMR) spectroscopy

Figure 6.29shows the NMR spectrum of HA & CMHA. The NMR spectrum of synthesized CMHA was compared with standard HA spectrum. The obtained NMR spectrum of HA showed signals of the protons of sugar ring between 2-3 ppm. In case of NMR of CMHA, new peaks were found between 2.5-3.5 ppm and also increased intensity of signal was found at 8.22 ppm which is due to the presence of –COOH group. All these noticeable changes confirmed carboxymethylation of HA [49, 50].

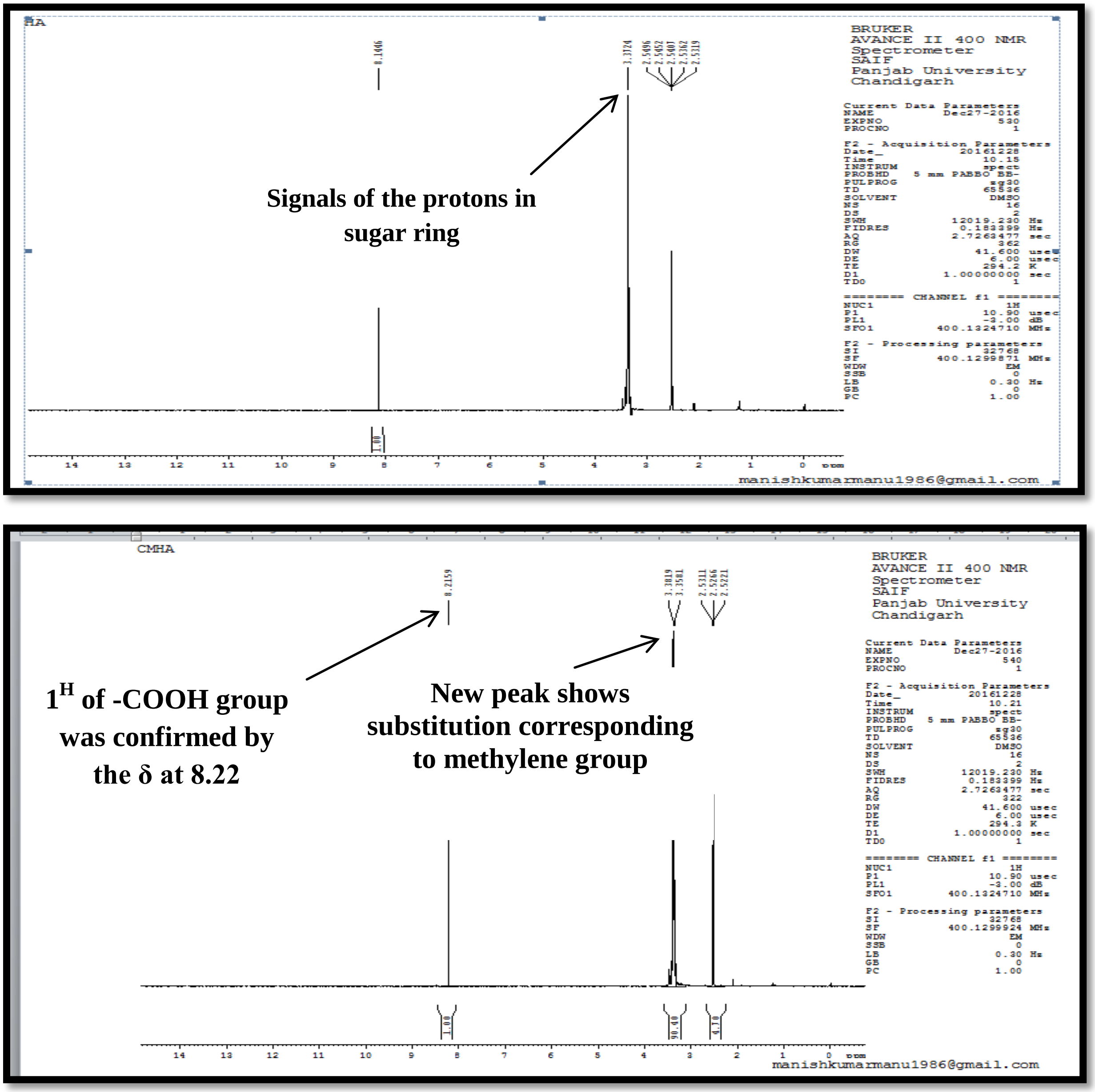

Figure 6.30: NMR spectra of (A) HA; (B) CMHA

6.8. CMHA-Lenalidomide conjugates

The extent of LND conjugation on CMHA was determined by measuring amount of unconjugated LND using ultraviolet (UV) spectrophotometric analysis. The optimization of conjugation was done to get maximum yield of conjugates (Table 6.17).

Table 6.17: Optimization of Conjugation Efficiency of CMHA-Lenalidomide Conjugates

Amount of LND added (mg) (Drug : Polymer)	**Amount of unconjugated LND (mg)**	**Amount of conjugated LND (mg)**	**% Conjugation Efficiency**
40 (2:5)	30.41	9.59	23.98
60 (3:5)	41.97	18.03	30.05
80 (4:5)	Precipitation of Drug		

Yield (mg)	110 ± 10.72 mg
% Yield ± SD	68.75 ± 6.7 %
Average amount of drug per 100 mg of CMHA-LND Conjugate (mg)	16.4 ± 1.59 mg
% Conjugation Efficiency ± SD	30.05 3.6 %

6.8.1. Infrared Spectroscopy of CMHA-Lenalidomide Conjugates

The IR spectrum (Table 6.18) of synthesized CMHA-LND Conjugates was compared with standard values of IR frequencies for different functional groups like Hydrazone bond. The obtained IR spectrum of CMHA–LND Conjugates showed all characteristic peaks of LND. Hence, formation of CMHA-LND Conjugate was confirmed [51].

Table 6.18: FT-IR spectra of CMHA-drug conjugate

Reported Frequency(cm^{-1})	**Observed Frequency(cm^{-1})**	**Inference**
3500-3100	3290	N-H bond Stretching(Hydrazone)
2900-3100	2945	Aromatic C-H Str.
1680-1750	1735	NH-NH_2 bond
1613-1631	1637	C=N bond

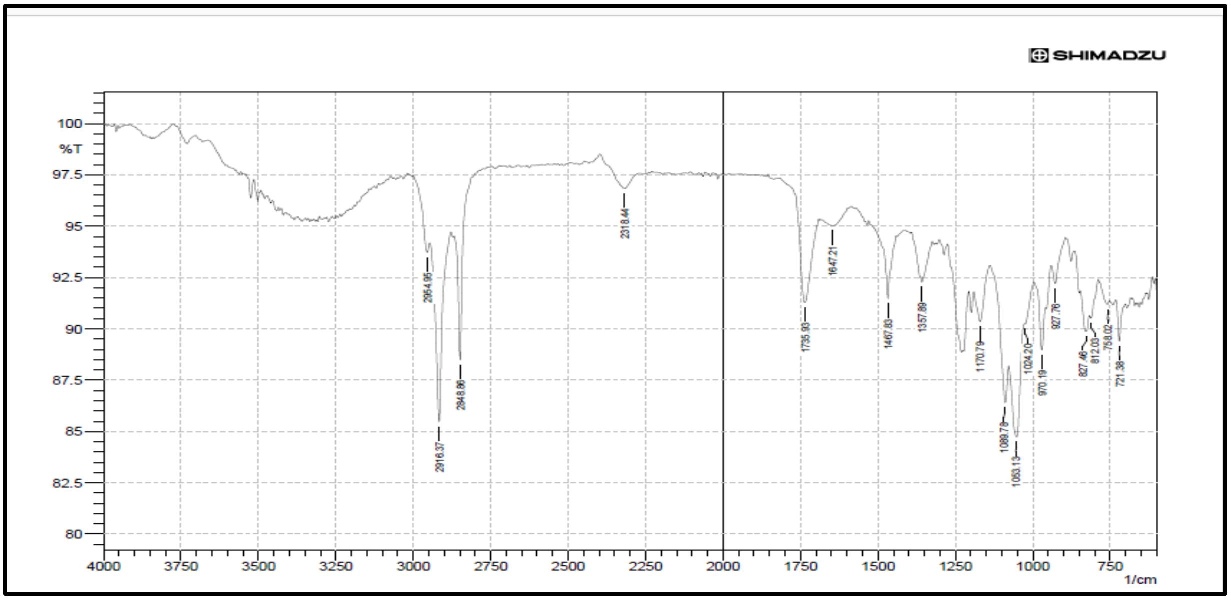

Figure 6.31: FT-IR spectra of CMHA-LND conjugate

6.8.2. NMR spectroscopy of CMHA-drug conjugate

The obtained NMR spectrum of CMHA-LND Conjugate showed the presence of a signal in the ^{1}H NMR spectra in the region of 8-15 ppm which gives evidence of the presence of an ArNH fragment and confirms the hydrazone structure (Figure 6.32). Furthermore, the downfield shift of this signal is characteristic for the formation of an intra-molecular hydrogen bond of the NH proton. The amide proton (-NH-C=O) is found back as a singlet at δ 10.21 All these noticeable changes confirmed carboxymethylation of HA [52].

6.8.3. DSC thermogram of CMHA-LND Conjugate

As evident from figure 6.33 (A), LND showed a sharp peak at 268.05˚C.The thermogram of CMHA-LND Conjugates (Figure 6.33 (B)) did not show any peak of LND. This shows that LND is completely conjugated without any traces of drug on the surface of the conjugate. Small peak around 200˚C was observed in DSC thermogram of CMHA-LND Conjugate which could be due to melting of Hydrazone containing compound [53].

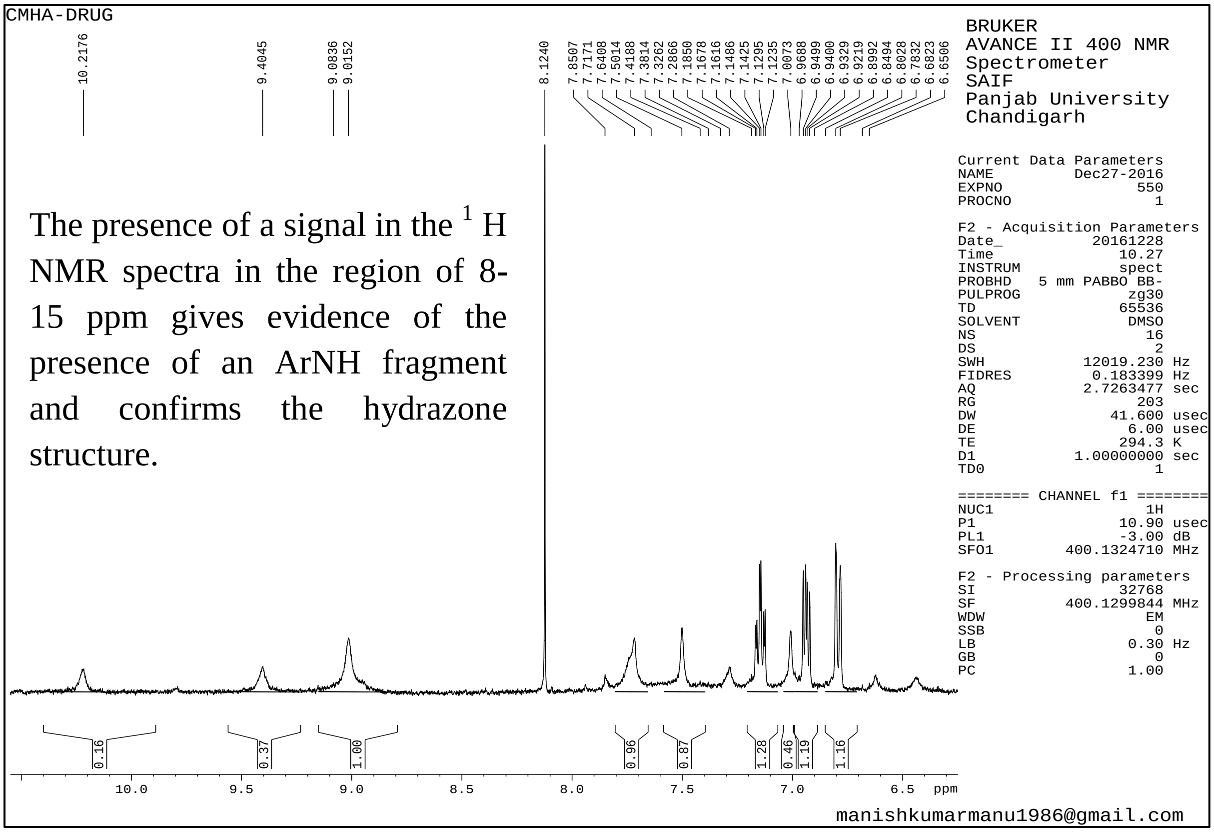

The presence of a signal in the ^{1}H NMR spectra in the region of 8-15 ppm gives evidence of the presence of an ArNH fragment and confirms the hydrazone structure.

```
BRUKER
AVANCE II 400 NMR
Spectrometer
SAIF
Panjab University
Chandigarh

Current Data Parameters
NAME         Dec27-2016
EXPNO               550
PROCNO                1

F2 - Acquisition Parameters
Date_          20161228
Time              10.27
INSTRUM           spect
PROBHD   5 mm PABBO BB-
PULPROG            zg30
TD                65536
SOLVENT            DMSO
NS                   16
DS                    2
SWH           12019.230 Hz
FIDRES         0.183399 Hz
AQ            2.7263477 sec
RG                  203
DW               41.600 usec
DE                 6.00 usec
TE                294.3 K
D1           1.00000000 sec
TD0                   1

======== CHANNEL f1 ========
NUC1                 1H
P1                10.90 usec
PL1               -3.00 dB
SFO1        400.1324710 MHz

F2 - Processing parameters
SI                32768
SF          400.1299844 MHz
WDW                  EM
SSB                   0
LB                 0.30 Hz
GB                    0
PC                 1.00
```

manishkumarmanu1986@gmail.com

Figure 6.32: NMR spectrum of CMHA-drug conjugate

6.8.4. XRD Analysis

X-ray powder diffraction was employed to confirm the degree of crystallinity of the ADNs. The XRD spectra of LND, CMHA, CMHA-LND Conjugates, and Fe_2O_3@FePt-CMHA-LND conjugates are shown in figure 6.34. The XRD spectrum of pure LND indicated that the drug is crystalline in nature. XRD spectrum of CMHA, CMHA-LND Conjugates, demonstrated that they were amorphous in nature with some characteristic peaks of LND and HA. XRD spectrum of Fe_2O_3@FePt-CMHA-LND conjugates showed characteristic peaks of Fe but absence of characteristic peaks of LND was observed which suggested absence of free drug [54].

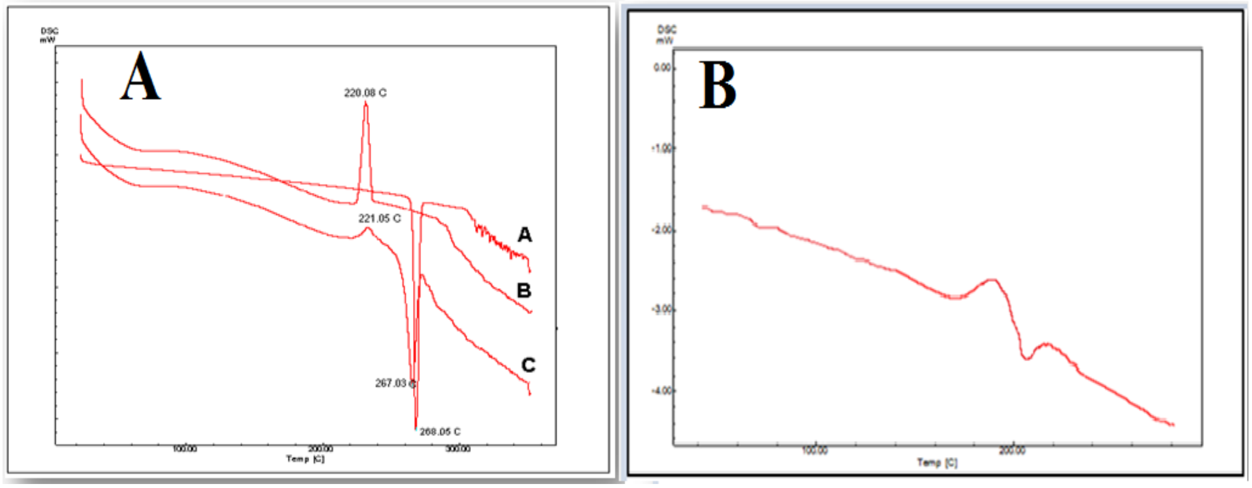

Figure 6.33:(A) DSC curve of (A) LND; (B) Hyaluronic acid; (C) Fe_2O_3@FePt-HA@LND nanoconjugates; (B) DSC curve of CMHA-LND conjugates

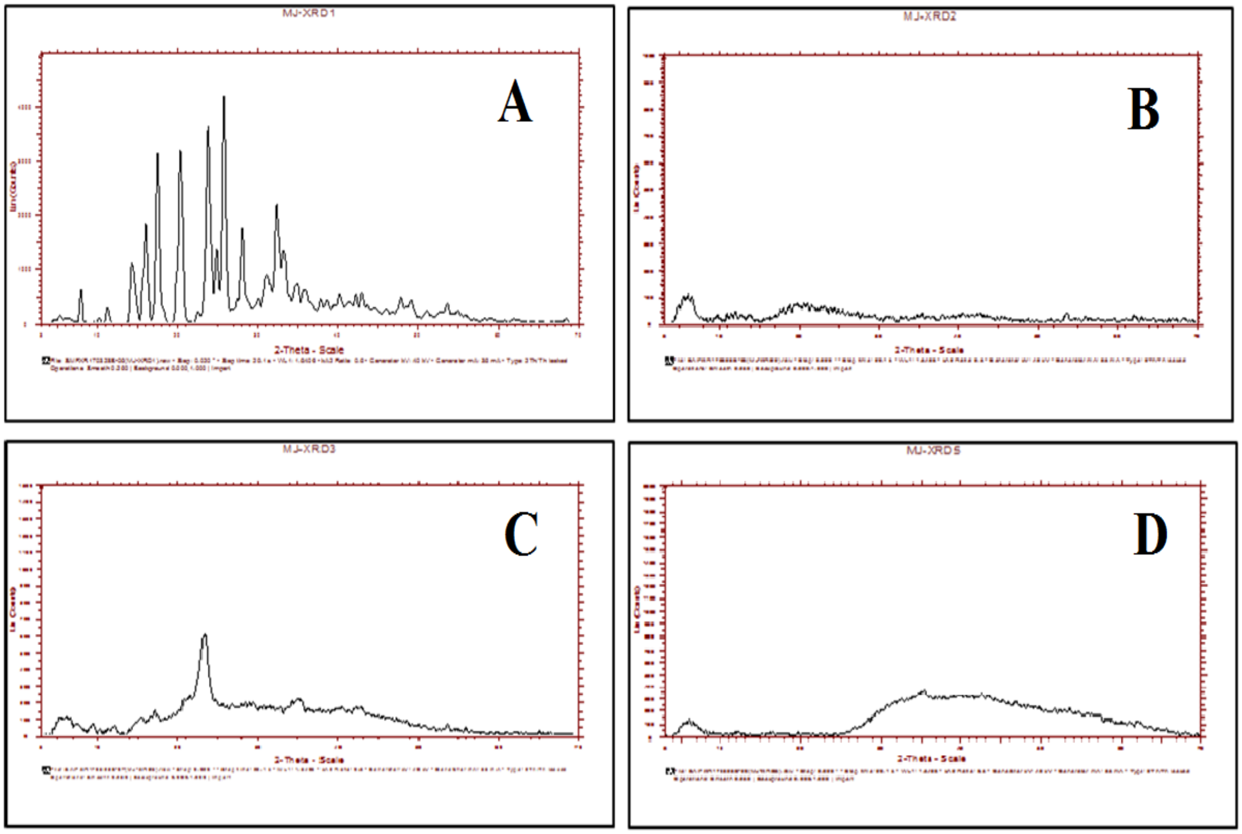

Figure 6.34: XRD plot of (A) LND, (B) CMHA, (C) CMHA-LND Conjugates, and (D) Fe_2O_3@FePt-CMHA-LND conjugates.

6.9. Electron Spin Resonance analysis of Fe_2O_3@FePt Nanoparticles

ESR curves for Fe_2O_3@FePt Nanoparticles and Fe_2O_3@FePt-CMHA-LND nanoparticles (Figure 6.35) demonstrated that the intensity of the curve for Fe_2O_3@FePt Nanoparticles was more that ofFe_2O_3@FePt-CMHA-LND nanoparticles. This can be attributed to the fact that conjugation of HA enhances biocompatibility of Fe_2O_3@FePt nanoparticles by increasing steric hindrance for biomolecules to interact freely with Fe_2O_3@FePt nanoparticles which is responsible for production of ROS .After cellular uptake of Fe_2O_3@FePt-CMHA-LND, the HA layer will be removed, causing enhanced release of Fe ions from Fe_2O_3@FePt nanoparticles leading to production of ROS and death of cancer cells ensuring less harm to non-cancerous cells [55].

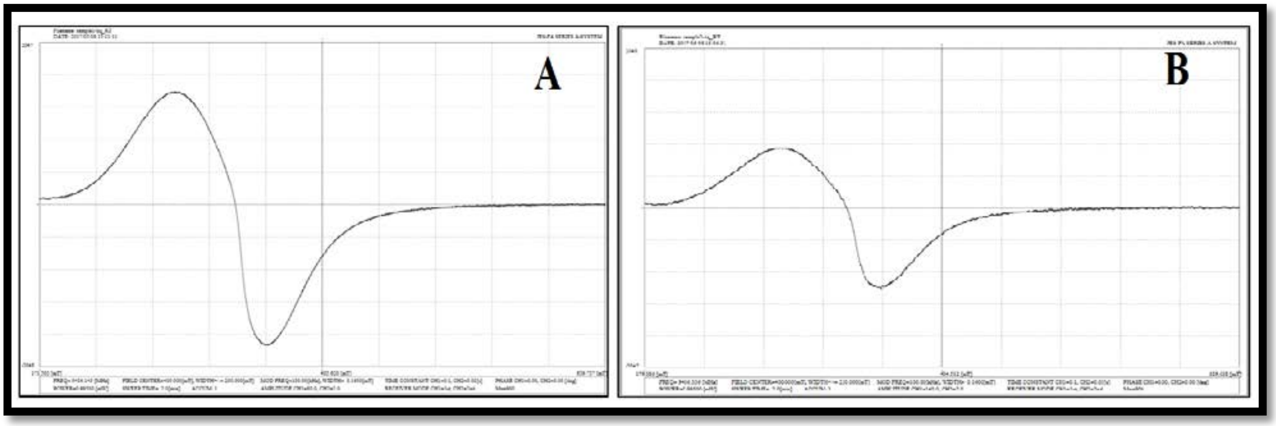

Figure 6.35: ESR curves for (A) Fe_2O_3@FePt Nanoparticles and (B) Fe_2O_3@FePt-CMHA-LND nanoparticles

6.10. Calculation and Optimization of Drug loading efficiency

Drug loading efficiency was calculated by finding out the amount of CMHA Lenalidomide conjugates present in the total amount of Fe_2O_3@FePt-Drug Nanoconjugates.From the table 6.19, it is clear that no significant change in loading efficiency was observed with increase in the amount of CMHA drug conjugate. This can be due to limited number of functional groups present on nanoparticles which can bind to CMHA drug conjugate. At 120 mg concentration of CMHA drug conjugate, maximum loading efficiency was obtained after which no significant increase in loading efficiency was observed with increase in CMHA drug conjugate. Hence, 100mg of nanoparticles and 120mg of Conjugates were taken for preparation of final batch.

Table 6.19: Calculation and Optimization of Drug Loading

Initial amount of nanoparticles taken (mg)	Initial amount of conjugates taken (mg)	Yield (mg)	Total amount of drug present (mg)	% Drug Loading
100	100	190	14.75	7.763
100	120	214	18.69	8.732
100	140	218	19.34	8.872

6.11. LND Release in Tumor Mimicking Environment

The pH responsive drug release from drug loaded Fe_2O_3@FePt was demonstrated at pH 7.4, 6.5, 5.5 and 4.8 corresponding to cytoplasm, early endosomes, late endosomes and lysozome respectively, while Fe release was performed at pH 7.4 and 4.8 as nanoparticles have maximum residence time in these two pH environment (Figure 6.36). Notably, an enhanced drug release was observed in acidic pH while very less release was observed in pH 7.4 and pH 6.5. The increased drug release in acidic conditions was due to lysis of pH labile hydrazone bonding between drug and nanoparticles (The stability of hydrazone bonding was assessed using *in vitro* technique in which pH sensitive Fe_2O_3@FePt-LND conjugates were incubated in pH 7.4 PBS and pH 4.8 acetate buffer for 2h. No significant drug release was observed in PBS while almost 10% release of LND occurred in pH 4.8). While after 12 h only 9.5%±1.7 and 12.2%±2.9% drug release was observed at pH 7.4 and 6.5 respectively, 24.4%±2.4% and 19.3%±2.9% drug release was observed after 12 h at pH 5.5 and 4.8 respectively. More than 52.6%±3.9% drug release was analyzed at pH 5.5 after 48h while around 40.4%±4.2% drug release was observed at pH 4.8. Drug release at pH 6.5 and 7.4 was approximately 18.7%±3.9% after 48 h. The decreased release of drug from Fe_2O_3@FePt at pH 7.4 demonstrates that toxicity to normal cells will be minimal as very less quantity of drug will be released during circulation of Fe_2O_3@FePt in blood and CSF (cerebrospinal fluid) as both have pH of 7.4.

The Fe release from Fe_2O_3@FePt was very less in the first 6 h in both pH 7.4 (1.3%±0.7%) and 4.8 (5.2%±1.7%). A sudden increase in Fe release was observed after 8 h in pH 4.8 (12.3%±1.4%) while in pH 7.4 (1.3%±0.7%) the increase in Fe release was insignificant. The slow release of Fe demonstrates that FePt in Fe_2O_3@FePt acts as a reservoir of Fe which is not the case with iron oxide nanoparticles. The release of Fe after 24 h was 18.7%±2.9% at pH 4.8, while it was only 3.7%±1.3% at pH 7.4 implying that Fe will not be released in neutral pH (plasma and CSF) where as high concentration will be available in lysozome of cancer cells due to acidic pH. The release of Fe can be further controlled by modulating the elemental composition of FePt nanoparticles in Fe_2O_3@FePt. With increase in Fe content in FePt nanoparticles, increase in Fe release can be obtained.

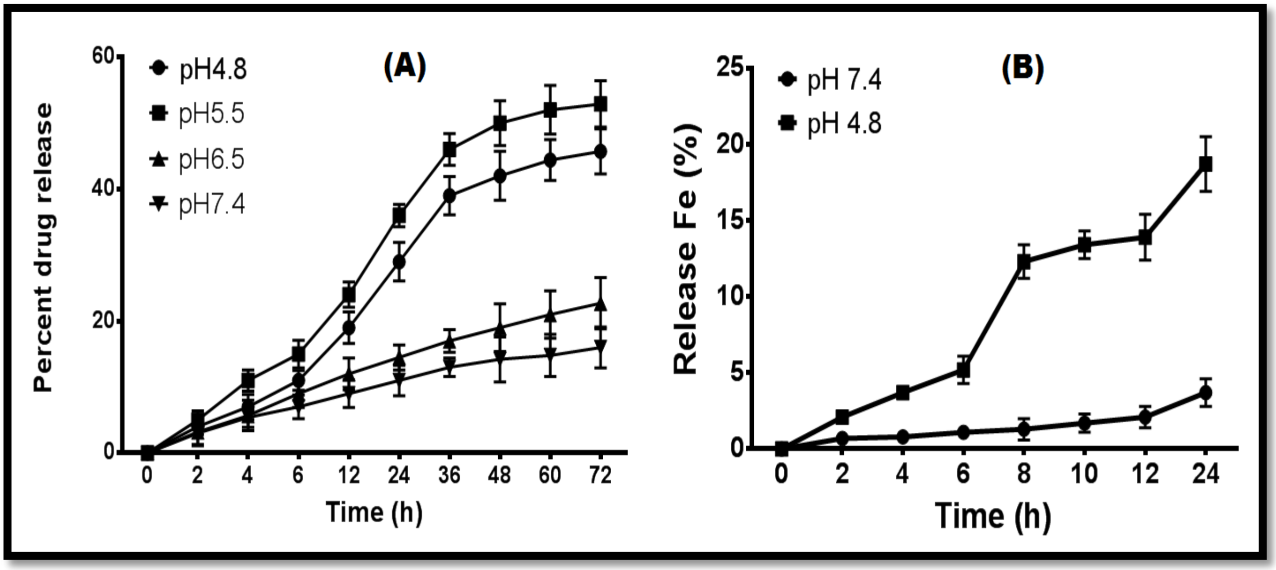

Figure 6.36: Graph showing (A) drug release and (B) release of Fe from Fe_2O_3@FePt nanoparticles.

6.12. Mucus penetration Study

The cumulative intensity of FITC SPANs and FITC conjugated M-SPANs through the mucus layer demonstrated more than 80.4%±5.3% and 82.5%%±4.7% penetration across mucus layer after 90min.

Table 6.20: Mucus penetrating ability of SPANs

Sr. No.	Nanoparticles	% Penetration 0min	30min	60min	90min
1	SPANs	0±0	34.7±2.7	77.6±2.7	80.4±5.3
2	M-SPANs	0±0	37.6±2.9	80.1±1.9	82.5±4.7

FITC was transferred respectively across mucus membrane after 90 min. The obtained results (Table 6.20) demonstrate efficient transfer of SPANs and M-SPANs across the mucus membrane. The result also suggests absence of significant interaction between mucin and SPANs.

6.13. Interactions

The interaction of nanoparticles in various biological media plays an important role in deciding the fate of nanoparticles and its delivery purpose. The interaction of surface modified Fe_2O_3@FePt was done to assessthe change in surface conditions of surface modified Fe_2O_3@FePt nanoparticles in presence of mucin, ECM and plasma. The results are shown in Table 6.21, 6.22 and 6.23.

Table 6.21: Interaction of surface modified Fe_2O_3@FePt nanoparticles with Mucin.

Sr. No.	**Nanoparticles**	**Particle size (nm)**		**Zeta Potential (mV)**	
		Initial	**Final**	**Initial**	**Final**
1	Fe_2O_3@FePt-NH_2-HA	9.4±1.3	9.7±1.4	12.7±2.6	13.2±2.2
2	Fe_2O_3@FePt-NH_2-FITC	9.3±1.1	10.1±1.2	-11.2±1.9	-9.7±1.2
3	Fe_2O_3@FePt-NH_2/COOH	9.1±1.2	9.4±1.1	-12.8±2.1	-10.7±2.2
4	Fe_2O_3@FePt-NH_2-TPP	11.2±1.3	11.8±1.4	45.6±2.9	46.9±2.5
5	Fe_2O_3@FePt-NH_2-TPP-COOH	11.7±1.5	11.9±1.2	38.4±2.7	39.7±2.6
6	Fe_2O_3@FePt-NH_2-TPP-COOH-Ctx	14.5±1.8	15.7±1.8	43.7±3.1	46.5±2.8
7	Fe_2O_3@FePt-NH_2/COOH-Drug	19.7±1.7	20.1±1.5	25.7±2.4	25.9±2.1
8	Fe_2O_3@FePt-NH_2-TPP-COOH-Drug	22.3±1.6	23.5±1.2	38.3±2.4	40.1±2.3
9	Fe_2O_3@FePt-COOH-DOTA-NH_2	15.1±1.3	15.6±1.1	29.7±2.5	28.5±2.4
10	Fe_2O_3@FePt-NH_2-DOTA-NCS	14.8±1.1	15.4±1.2	31.5±3.2	30.1±3.1
11	Fe_2O_3@FePt-NH_2/COOH-TPP-Drug-HA-Ctx	27.4±2.1	27.9±2.3	35.1±2.9	38.7±2.5
12	Fe_2O_3@FePt-NH_2/COOH-TPP-Drug-HA-Ctx (pH sensitive)	29.6±1.9	31.2±1.8	37.2±1.7	40.5±1.5

No significant interaction was observed except for nanoparticles modified with Ctx. This can be attributed to the fact that Ctx being a peptide attracts biomolecules toward it owing to hydrophobic interaction between its peptide chain and other biomolecules [55].The result suggests absence of significant interaction between mucin and surface modified Fe_2O_3@FePt nanoparticles as no significant change in zeta potential was observed although slight increase in particle size was observed which can be attributed to the interaction between negatively charged sialic acid residue of mucin and positively charged surface modified Fe_2O_3@FePt nanoparticles. The insignificant interaction between surface modified Fe_2O_3@FePt nanoparticles and mucin demonstrate that the nanoparticles won't get entangled in mucin which can hamper their mucus penetration.

Table 6.22: Interaction of surface modified Fe_2O_3@FePt nanoparticles with ECM.

Sr. No.	**Nanoparticles**	**Particle size (nm)**		**Zeta Potential (mV)**	
		Initial	**Final**	**Initial**	**Final**
1	Fe_2O_3@FePt-NH_2-HA	9.4±1.3	9.5±1.3	12.7±2.6	12.2±2.1
2	Fe_2O_3@FePt-NH_2-FITC	9.3±1.1	10.3±1.1	-11.2±1.9	-9.9±1.3
3	Fe_2O_3@FePt-NH_2/COOH	9.1±1.2	9.5±1.2	-12.8±2.1	-11.5±2.4
4	Fe_2O_3@FePt-NH_2-TPP	11.2±1.3	11.5±1.3	45.6±2.9	44.6±2.1
5	Fe_2O_3@FePt-NH_2-TPP-COOH	11.7±1.5	13.7±1.1	38.4±2.7	41.5±2.2
6	Fe_2O_3@FePt-NH_2-TPP-COOH-Ctx	14.5±1.8	15.5±1.7	43.7±3.1	47.2±2.3
7	Fe_2O_3@FePt-NH_2/COOH-Drug	19.7±1.7	21.4±1.1	25.7±2.4	27.3±2.9
8	Fe_2O_3@FePt-NH_2-TPP-COOH-Drug	22.3±1.6	23.9±1.5	38.3±2.4	41.5±2.3
9	Fe_2O_3@FePt-COOH-DOTA-NH_2	15.1±1.3	16.2±1.1	29.7±2.5	30.9±2.5
10	Fe_2O_3@FePt-NH_2-DOTA-NCS	14.8±1.1	15.2±1.4	31.5±3.2	31.7±3.1
11	Fe_2O_3@FePt-NH_2/COOH-TPP-Drug-HA-Ctx	27.4±2.1	30.7±2.5	35.1±2.9	41.5±2.1
12	Fe_2O_3@FePt-NH_2/COOH-TPP-Drug-HA-Ctx (pH sensitive)	29.6±1.9	32.5±1.9	37.2±1.7	41.4±1.4

Table 6.23: Interaction of surface modified Fe_2O_3@FePt nanoparticles with Plasma

Sr. No.	Nanoparticles	Particle size (nm)		Zeta Potential (mV)	
		Initial	Final	Initial	Final
1	Fe_2O_3@FePt-NH_2-HA	9.4±1.3	10.5±1.4	12.7±2.6	15.3±1.9
2	Fe_2O_3@FePt-NH_2-FITC	9.3±1.1	10.1±1.1	-11.2±1.9	-10.8±1.4
3	Fe_2O_3@FePt-NH_2/COOH	9.1±1.2	9.9±1.3	-12.8±2.1	-13.4±2.3
4	Fe_2O_3@FePt-NH_2-TPP	11.2±1.3	12.3±1.5	45.6±2.9	47.4±2.6
5	Fe_2O_3@FePt-NH_2-TPP-COOH	11.7±1.5	12.7±1.2	38.4±2.7	40.9±2.1
6	Fe_2O_3@FePt-NH_2-TPP-COOH-Ctx	14.5±1.8	16.9±1.7	43.7±3.1	46.3±2.7
7	Fe_2O_3@FePt-NH_2/COOH-Drug	19.7±1.7	21.7±1.5	25.7±2.4	26.4±2.3
8	Fe_2O_3@FePt-NH_2-TPP-COOH-Drug	22.3±1.6	23.9±1.3	38.3±2.4	42.1±2.3
9	Fe_2O_3@FePt-COOH-DOTA-NH_2	15.1±1.3	15.9±1.7	29.7±2.5	31.3±2.7
10	Fe_2O_3@FePt-NH_2-DOTA-NCS	14.8±1.1	15.9±1.3	31.5±3.2	33.5±3.2
11	Fe_2O_3@FePt-NH_2/COOH-TPP-Drug-HA-Ctx	27.4±2.1	29.5±2.4	35.1±2.9	38.9±2.4
12	Fe_2O_3@FePt-NH_2/COOH-TPP-Drug-HA-Ctx (pH sensitive)	29.6±1.9	33.1±1.7	37.2±1.7	42.5±1.9

6.14. Hemocompatibility and Haemolysis Study

Results of hemocompatibility study of surface modified Fe_2O_3@FePt nanoparticles confirmed no significant biological interaction with any of blood components. The % Haemolysis was found to be 1.35% for Fe_2O_3@FePt nanoparticles and 1.42% for Fe_2O_3@FePt-NH_2/COOH-TPP-Drug-HA-Ctx nanoparticles. The value of % Haemolysis was<2% for both nanoparticles which suggest non hemolytic activity of synthesized nanoparticles [56]. The Value of % Haemolysis of surface modified nanoparticles was also <2% confirming hemocompatibility of surface modified nanoparticles (Table 6.24).

Table 6.24: Results of % Haemolysis by surface modified Fe_2O_3@FePt nanoparticles

Sr. No.	Nanoparticles	% Hemolysis
1	Fe_2O_3@FePt-NH_2-HA	0.9
2	Fe_2O_3@FePt-NH_2-FITC	1.19
3	Fe_2O_3@FePt-NH_2/COOH	1.12
4	Fe_2O_3@FePt-NH_2-TPP	1.87
5	Fe_2O_3@FePt-NH_2-TPP-COOH	1.21
6	Fe_2O_3@FePt-NH_2-TPP-COOH-Ctx	1.17
7	Fe_2O_3@FePt-NH_2/COOH-Drug	1.29
8	Fe_2O_3@FePt-NH_2-TPP-COOH-Drug	1.32
9	Fe_2O_3@FePt-COOH-DOTA-NH_2	1.13
10	Fe_2O_3@FePt-NH_2-DOTA-NCS	1.48
11	Fe_2O_3@FePt-NH_2/COOH-TPP-Drug-HA-Ctx	1.42
12	Fe_2O_3@FePt-NH_2/COOH-TPP-Drug-HA-Ctx (pH sensitive)	1.38

6.15. Stability Studies

The cellular uptake of nanoparticles depends on their surface charge and particle size. Variation in particle size and surface potential during study might cause variation and error in obtained results. To minimize error while performing cell line studies, stability of synthesized nanoparticles was studied in cell culture medium (DMEM) to assess presence or absence of aggregate formation. The stability of synthesized nanoparticles was also assessed in simulated nasal fluid to understand behavior of nanoparticles after nasal administration during *in vivo* studies.

From the obtained results (Table 6.25) demonstrate absence of any significant change in particle size or surface potential in DMEM. Similar to DMEM, no significant variation in particle size or surface potential was observed in case of SNF (results not shown).

Table 6.25: Stability of surface modified Fe_2O_3@FePt nanoparticles in DMEM

Sr. No.	Nanoparticles	Particle size (nm)		Zeta Potential (mV)	
		Initial	Final	Initial	Final
1	Fe_2O_3@FePt-NH_2-HA	9.4±1.3	9.7±1.2	12.7±2.6	12.9±1.7
2	Fe_2O_3@FePt-NH_2-FITC	9.3±1.1	9.5±1.2	-11.2±1.9	-11.4±1.1
3	Fe_2O_3@FePt-NH_2/COOH	9.1±1.2	9.3±1.3	-12.8±2.1	-13.1±2.5
4	Fe_2O_3@FePt-NH_2-TPP	11.2±1.3	11.3±1.5	45.6±2.9	45.9±2.3
5	Fe_2O_3@FePt-NH_2-TPP-COOH	11.7±1.5	11.9±1.1	38.4±2.7	38.9±1.9
6	Fe_2O_3@FePt-NH_2-TPP-COOH-Ctx	14.5±1.8	14.9±1.4	43.7±3.1	44.3±2.3
7	Fe_2O_3@FePt-NH_2/COOH-Drug	19.7±1.7	20.1±1.1	25.7±2.4	26.1±2.8
8	Fe_2O_3@FePt-NH_2-TPP-COOH-Drug	22.3±1.6	22.7±1.4	38.3±2.4	39.8±2.2
9	Fe_2O_3@FePt-COOH-DOTA-NH_2	15.1±1.3	15.5±1.5	29.7±2.5	30.3±2.7
10	Fe_2O_3@FePt-NH_2-DOTA-NCS	14.8±1.1	14.9±1.2	31.5±3.2	31.5±1.7
11	Fe_2O_3@FePt-NH_2/COOH-TPP-Drug-HA-Ctx	27.4±2.1	27.5±2.1	35.1±2.9	35.9±2.8
12	Fe_2O_3@FePt-NH_2/COOH-TPP-Drug-HA-Ctx (pH sensitive)	29.6±1.9	30.1±1.3	37.2±1.7	37.8±2.9

6.16. Nanoparticles and Protein Corona

Ni significant variation in particle size and surface potential was observed after 48h incubation confirming absence of formation of protein corona over SPANs and M-SPANs.

Table 6.26: Nanoparticles and Protein Corona

Sr. No.	Nanoparticles	Particle size (nm)					Zeta Potential (mV)				
		0h	6h	12h	24h	48h	0h	6h	12h	24h	48h
1	SPANs	27.4±2.1	27.7±1.9	27.6±2.1	28.3±2.2	28.9±2.3	35.1±2.9	35.9±2.1	35.8±2.2	36.1±1.9	36.8±2.1
2	M-SPANs	29.6±1.3	29.8±1.4	30.1±1.7	30.5±1.9	30.9±2.4	37.2±1.7	37.5±1.2	37.8±1.7	38.2±2.4	39.5±2.7

References

1. R.K. Sharma, D. Kumar, P. Kumar. Systematic failure mode effect analysis (FMEA) using fuzzy linguistic modeling. International Journal of Quality& Reliability Management. 2005, 22(9),986-1004.
2. J.B. Bowles, An assessment of RPN prioritization in a failure modes effects and criticality analysis. Reliability and Maintainability Symposium, 2003 Annual, 2003, IEEE.
3. M. Bloemen, W. Brullot, T.T. Luong, N. Geukens, A. Gils, T. Verbiest, Improved functionalization of oleic acid-coated iron oxide nanoparticles for biomedical applications. Journal of Nanoparticle Research. 2012, 14(9), 1100-1109.
4. Y. Xia, Y. Xiong, B. Lim, S.E. Skrabalak. Shape-controlled synthesis of metal nanocrystals: Simple chemistry meets complex physics. Angewandte Chemie International Edition. 2009, 48(1), 60-103.
5. P.R. Sajanlal, T.S. Sreeprasad, A.K. Samal, T. Pradeep. Anisotropic nanomaterials: structure, growth, assembly, and functions. Nano reviews. 2011, 2(1), 5883-5892.
6. A. Crocker, J. Akhter, H. Tatham, Point defect interactions with crystal interfaces. Surface Science. 1984, 144(1), 96-109.
7. D. Singh, J.M. McMillan, X.-M. Liu, H.M. Vishwasrao, A.V. Kabanov, M. Sokolsky-Papkov, et al. Formulation design facilitates magnetic nanoparticle delivery to diseased cells and tissues. Nanomedicine.2014, 9(3), 46985-46992.
8. https://www.ich.org/fileadmin/Public_Web_Site/ICH_Products/Guidelines/Quality/Q8_R1/Step4/Q8_R2_Guideline.pdf
9. A.P. Pandey, K.P. Karande, R.O. Sonawane, P.K. Deshmukh, Applying quality by design (QbD) concept for fabrication of chitosan coated nanoliposomes. Journal of Liposome Research. 2014, 24(1), 37-52.
10. A.P. Pandey, M.P. More, K.P. Karande, R.V. Chitalkar, P.O. Patil, P.K. Deshmukh, Optimization of desolvation process for fabrication of lactoferrin nanoparticles using quality by design approach. Artificial cells, Nanomedicine, and Biotechnology. 2017, 45(6),1101-1114.

11. S. Sun, C.B. Murray, D. Weller, L. Folks, A. Moser, Monodisperse FePt nanoparticles and ferromagnetic FePt nanocrystal superlattices. Science. 2000, 287(5460), 1989-1992.
12. B. Bouchet, J.M. Martin, J. Avila, M. Kano, K. Yoshida, T. Tsuruda, et al. Diamond-like carbon coating under oleic acid lubrication: Evidence for graphene oxide formation in superlow friction. Scientific Reports. 2017,7, 1-12.
13. W. Jiang, Y. Wu, B. He, X. Zeng, K. Lai, Z. Gu, Effect of sodium oleate as a buffer on the synthesis of superparamagnetic magnetite colloids. Journal of Colloid and Interface Science. 2010, 347(1),1-7.
14. R.A. Harris, P.M. Shumbula, H.t. van der Walt. Analysis of the interaction of surfactants oleic acid and oleylamine with iron oxide nanoparticles through molecular mechanics modeling. Langmuir. 2015, 31(13), 3934-3943.
15. D.P. Joshi, G. Pant, N. Arora, S. Nainwal, Effect of solvents on morphology, magnetic and dielectric properties of (α-Fe2O3@ SiO2) core-shell nanoparticles. Heliyon. 2017,3(2),e00253-00259.
16. E. Soto-Cantu, R. Cueto, J. Koch, P.S. Russo, Synthesis and rapid characterization of amine-functionalized silica. Langmuir. 2012, 28(13), 5562-5569.
17. Q.X. Nguyen, T.G. Belgard, J.J. Taylor, V.S. Murthy, N.J. Halas, M.S. Wong, Water-phase synthesis of cationic silica/polyamine nanoparticles. Chemistry of Materials. 2012, 24(8),1426-33.
18. R.J. Soto, L. Yang, M.H. Schoenfisch, Functionalized mesoporous silica via an aminosilane surfactant ion exchange reaction: controlled scaffold design and nitric oxide release. ACS Applied Materials & Interfaces. 2016, 8(3), 2220-2231.
19. N.J. Kavimandan, E. Losi, J.J. Wilson, J.S. Brodbelt, N.A. Peppas, Synthesis and Characterization of Insulin− Transferrin Conjugates. Bioconjugate Chemistry. 2006, 17(6), 1376-1384.
20. A.P. Pandey, K.K. Sawant. Polyethylenimine: A versatile, multifunctional non-viral vector for nucleic acid delivery. Materials Science and Engineering: C. 2016, 68, 904-918.
21. A.W. Eyl, T. Inagami, Identification of essential carboxyl groups in the specific binding site of bovine trypsin by chemical modification. Journal of Biological Chemistry. 1971, 246(3),738-746.

22.M. Zhou, Z. Wei, H. Qiao, L. Zhu, H. Yang, T. Xia, Particle size and pore structure characterization of silver nanoparticles prepared by confined arc plasma. Journal of Nanomaterials. 2009, 2009,1-7.

23. Y. Liu, K. Yang, L. Cheng, J. Zhu, X. Ma, H. Xu, et al. PEGylated FePt@ Fe 2 O 3 core-shell magnetic nanoparticles: potential theranostic applications and in vivo toxicity studies. Nanomedicine: Nanotechnology, Biology and Medicine. 2013, 9(7),1077-1088.

24. H.L. Nguyen, L.E. Howard, G.W. Stinton, S.R. Giblin, B.K. Tanner, I. Terry, et al. Synthesis of size-controlled fcc and fct FePt nanoparticles. Chemistry of materials. 2006, 18(26), 6414-6424.

25. C. Dablemont, P. Lang, C. Mangeney, J.-Y. Piquemal, V. Petkov, F. Herbst, et al. FT-IR and XPS study of Pt nanoparticle functionalization and interaction with alumina. Langmuir. 2008, 24(11), 5832-5841.

26. M. Ma, P. Bourges, Y. Sidis, Y. Xu, S. Li, B. Hu, et al. Prominent role of spin-orbit coupling in FeSe. Physical Review X. 2017, 7, 021025-021029

27. A. Akbarzadeh, M. Samiei, S. Davaran, Magnetic nanoparticles: preparation, physical properties, and applications in biomedicine. Nanoscale Research Letters. 2012, 7(1), 144-149.

28. Y. Zheng, Y. Tang, Z. Bao, H. Wang, F. Ren, M. Guo, et al., FePt nanoparticles as a potential X-ray activated chemotherapy agent for hela cells. International Journal of Nanomedicine. 2015, 10, 6435-6440

29. Y. Liu, K. Yang, L. Cheng, J. Zhu, X. Ma, H. Xu, et al., PEGylated FePt@ Fe 2 O 3 core-shell magnetic nanoparticles: potential theranostic applications and in vivo toxicity studies. Nanomedicine: Nanotechnology, Biology and Medicine. 2013, 9(7),1077-1088.

30. J. Gao, G. Liang, J.S. Cheung, Y. Pan, Y. Kuang, F. Zhao, et al. Multifunctional yolk−shell nanoparticles: a potential MRI contrast and anticancer agent. Journal of American Chemical Society. 2008, 130(35),11828-11833.

31. C. Choi, S.-D. Seo, B.-K. Kim, D.-W. Kim. Enhanced lithium storage in hierarchically porous carbon derived from waste tea leaves. Scientific Reports. 2016, 6, 1-7.

32. A. Espinosa, R. Di Corato, J. Kolosnjaj-Tabi, P. Flaud, T. Pellegrino, C. Wilhelm, Duality of iron oxide nanoparticles in cancer therapy: amplification of heating efficiency

by magnetic hyperthermia and photothermal bimodal treatment. ACS nano. 2016, 10(2), 2436-2446.

33. S. Kang, D. Nikles, J. Harrell, Synthesis, chemical ordering, and magnetic properties of self-assembled FePt–Ag nanoparticles. Journal of Applied Physics. 2003, 93(10), 7178-7180.
34. S. Huang, G. Chen, M. Chaker, T. Ozaki, P. Tijssen, D. Ma. Fluorescent-magnetic multifunctional nanoparticles for imaging and drug delivery. Reviews in Nanoscience and Nanotechnology. 2013, 2(5), 346-364.
35. J. Shen, Y. Hu, M. Shi, N. Li, H. Ma, M. Ye, One step synthesis of graphene oxide−magnetic nanoparticle composite. The Journal of Physical Chemistry C. 2010, 114(3),1498-1503.
36. D.G. Meeker, S.V. Jenkins, E.K. Miller, K.E. Beenken, A.J. Loughran, A. Powless, et al. Synergistic photothermal and antibiotic killing of biofilm-associated Staphylococcus aureus using targeted antibiotic-loaded gold nanoconstructs. ACS Infectious Diseases. 2016, 2(4), 241-250.
37. A.S. Teja, P.-Y. Koh, Synthesis, properties, and applications of magnetic iron oxide nanoparticles. Progress in crystal growth and characterization of materials. 2009, 55(1), 22-45.
38. C.S. Kumar, F. Mohammad. Magnetic nanomaterials for hyperthermia-based therapy and controlled drug delivery. Advanced Drug Delivery Reviews. 2011, 63(9),789-808.
39. X.L. Liu, E.S.G. Choo, A.S. Ahmed, L.Y. Zhao, Y. Yang, R.V. Ramanujan, et al. Magnetic nanoparticle-loaded polymer nanospheres as magnetic hyperthermia agents. Journal of Materials Chemistry B. 2014,2(1),120-8.
40. E. Kim, K. Lee, Y.-M. Huh, S. Haam. Magnetic nanocomplexes and the physiological challenges associated with their use for cancer imaging and therapy. Journal of Materials Chemistry B. 2013, 1(6), 729-739.
41. S. Mornet, S. Vasseur, F. Grasset, E. Duguet. Magnetic nanoparticle design for medical diagnosis and therapy. Journal of Materials Chemistry. 2004, 14(14), 2161-2175.
42. A.D. Maxwell, T.-Y. Wang, L. Yuan, A.P. Duryea, Z. Xu, C.A. Cain. A tissue phantom for visualization and measurement of ultrasound-induced cavitation damage. Ultrasound in Medicine & Biology. 2010, 36(12), 2132-2143.

43. Y. Jin, C. Jia, S.-W. Huang, M. O'Donnell, X. Gao. Multifunctional nanoparticles as coupled contrast agents. Nature Communications. 2010, 1, 41-48.
44. S. Lee, R. G. Thomas, M. J. Moon, H. J. Park, In-K. Park, B.-Il Lee, Y. Y. Jeong, Near-Infrared Heptamethine Cyanine Based Iron Oxide Nanoparticles for Tumor Targeted Multimodal Imaging and Photothermal Therapy. Scientific Reports. 2017, 7, 1-9
34. N.-N. Dong, M. Pedroni, F. Piccinelli, G. Conti, A. Sbarbati, J.E. Ramírez-Hernández, et al. NIR-to-NIR two-photon excited CaF2: Tm3+, Yb3+ nanoparticles: multifunctional nanoprobes for highly penetrating fluorescence bio-imaging. ACS Nano. 2011, 5(11), 8665-8671.
35. E. C. Wang, A. Z. Wang. Nanoparticles and their applications in cell and molecular biology. Integrative Biology (Camb). 2014, 6(1), 9–26
36. Ž. Stojanović, K. Jeremić, S. Jovanović, M.D. Lechner. A comparison of some methods for the determination of the degree of substitution of carboxymethyl starch. Starch Stärke. 2005, 57(2),79-83.
37. Y. Jiao, X. Pang, G. Zhai. Advances in hyaluronic acid-based drug delivery systems. Current drug targets. 2016,17(6),720-30.
38. M.A. Serban, G. Yang, G.D. Prestwich, Synthesis, characterization and chondroprotective properties of a hyaluronan thioethyl ether derivative. Biomaterials. 2008, 29(10), 1388-1399.
39. C.E. Schanté, G. Zuber, C. Herlin, T.F. Vandamme, Chemical modifications of hyaluronic acid for the synthesis of derivatives for a broad range of biomedical applications. Carbohydrate polymers. 2011, 85(3), 469-489.
40. A. Mero, M. Campisi, Hyaluronic acid bioconjugates for the delivery of bioactive molecules. Polymers. 2014, 6(2), 346-369.
41. J. Carneiro, P.M. Döll-Boscardin, B.C. Fiorin, J.M. Nadal, P.V. Farago, J.P.d. Paula. Development and characterization of hyaluronic acid-lysine nanoparticles with potential as innovative dermal filling. Brazilian Journal of Pharmaceutical Sciences. 2016, 52(4), 645-651.
42. S. Zhai, Y. Ma, Y. Chen, D. Li, J. Cao, Y. Liu, et al. Synthesis of an amphiphilic block copolymer containing zwitterionic sulfobetaine as a novel pH-sensitive drug carrier. Polymer Chemistry. 2014, 5(4), 1285-1297.

43. A.M. Alanazi, A.S. Abdelhameed, A.H. Bakheit, I.A. Darwish. Exploring the interaction forces involved in the binding of the multiple myeloma drug lenalidomide to bovine serum albumin. Journal of Molecular Liquids. 2017, 238, 3-10.
44. S. Kwon. Applications of sortase A in disulfide-rich peptide engineering. 2016.
45. F.-Y. Cheng, C.-H. Su, Y.-S. Yang, C.-S. Yeh, C.-Y. Tsai, C.-L. Wu, et al. Characterization of aqueous dispersions of Fe 3 O 4 nanoparticles and their biomedical applications. Biomaterials. 2005, 26(7), 729-738.